

SEISMIC REFRACTION TO EXPLORE THE INFLUENCE OF BELOWGROUND
WATER STORAGE ON SAP FLOW VELOCITIES IN PINES

By

Emmalynn Hicks

A thesis submitted to the Faculty and the Board of Trustees of the Colorado School of Mines in partial fulfillment of the requirements for the degree of Master of Science (Hydrology).

Golden, Colorado

Date _____

Signed: _____
Emma Hicks

Signed: _____
Dr. Kamini Singha
Thesis Advisor

Golden, Colorado

Date _____

Signed: _____
Dr. David Benson
Professor and Director
Hydrologic Science and Engineering Program

ABSTRACT

Water storage in the critical zone acts as a buffer between trees and the effects of climate change by aiding in a tree community's ability to survive water scarcity. Consequently, predicting how subsurface water-storage patterns may change under a changing climate and how trees will respond to these changes is vital for accurately assessing tree mortality. Here, we conducted a study on two opposing slopes of Gordon Gulch in the Boulder Creek Critical Zone in Boulder, CO. Sap flow—which is used as a measure of tree productivity—and seismic refraction data were collected to explore how and if subsurface water storage is related to the productivity of ponderosa and lodgepole pine trees. Four sap flow plots, two on north-facing and two on south-facing slopes, each containing roughly 8 trees, were instrumented with sap flow sensors. There is a greater depth of saprolite and unconsolidated material on the north-facing slope of Gordon Gulch, where we see an abundance of tightly spaced lodgepole pine trees. The depth of the saprolite and unconsolidated layers on the south-facing slope are shallow in comparison to the north-facing slope with the south-facing slope consisting of sparsely spaced ponderosa pine trees. Three out of the four sap flow plots displayed seasonal trends with sap flow velocity values that appear to generally correspond to subsurface water storage capacity between sites on each slope, although it was clear other variables also controlled sap flow. Sap flow velocities differed between the two plots on the south-facing slope, which had the same tree species on them, indicating that differences in the thickness of water-holding materials and other environmental and biological factors, such as slope/aspect and rooting depth, likely influence sap flow differently between sites. Sap flow velocities decreased significantly following August for the south-facing upslope plot while they remained high for the downslope plot, leading us to speculate that belowground water storage potential might be positively influencing sap flow rates

into late summer. In short, we found that differences in water storage capacity may influence sap flow velocities but are convolved with other factors such as solar radiation, soil/rock moisture, and rooting depth.

TABLE OF CONTENTS

ABSTRACT.....	III
LIST OF FIGURES	VII
LIST OF TABLES	IX
LIST OF EQUATIONS	IX
ACKNOWLEDGEMENTS	X
CHAPTER 1 GENERAL INTRODUCTION	1
CHAPTER 2 SEISMIC REFRACTION TO EXPLORE THE INFLUENCE OF BELOWGROUND WATER STORAGE ON SAP FLOW VELOCITIES IN PINES.....	3
2.1 Abstract.....	3
2.2 Introduction.....	4
2.3 Site Description.....	7
2.4 Methods.....	13
2.4.1 Sap Flow Collection Methods	13
2.4.2 Seismic Refraction Survey Methods	15
2.4.3 Soil Moisture Methods.....	17
2.5 Results.....	17
2.5.1 Sap Flow Results	17
2.5.2 Seismic Results	18
2.5.3 Soil Moisture Results	20
2.6 Discussion.....	21
2.7 Conclusions.....	25
CHAPTER 3 FUTURE WORK.....	27
3.1 Increased Spatial Coverage.....	27
3.2 Additional Methods	28
3.3 Spectrograms and Wavelet Analysis	29
REFERENCES	31
APPENDIX A STACKING, PICKING, AND INVERTING SEISMIC DATA	36
A.1 Stack shots.....	36
A.1.1 Converting Data	36
A.1.2 Creating a Stacking Guide	37

A.1.3 Automated stacking with Python Script.....	39
A.2 Picking First Arrivals	42
A.3 Inverting with pyGIMLi.....	44
APPENDIX B ADDITIONAL FIGURES.....	47

LIST OF FIGURES

Figure 2.1	Map of the Gordon Gulch watershed with the field site outlined in a black dotted line, highlighting the location of our three seismic lines and four sap flow plots. The three seismic lines are labeled Lines 1, 2, & 3 (in blue), and the four sap flow plots are labeled SF_High, SF_Low, NF_High, NF_Low, with the green dots indicating the locations of the individual trees installed with sap flow sensors. Soil moisture probes were installed centrally at each of the sap flow plots.....	8
Figure 2.2	Images of the area near sap flow Plots A) NF_High and B) NF_Low on the north facing slope of Gordon Gulch.....	11
Figure 2.3	Images of the area near sap flow Plots A) SF_High and B) SF_Low on the south facing slope of Gordon Gulch.	12
Figure 2.4	Sap flow velocities for plots (A) SF_High and (B) SF_Low on the south-facing slope and (C) NF_High on the north-facing slope from June-September 2021. The gray lines are sap flow collected for each tree at each plot and the black lines are the average sap flow velocities of all individual trees at each plot.....	18
Figure 2.5	P-wave velocities for the three seismic lines with the start and end of the sap flow plots shown as green trees. A) Line 1 on the south-facing slope and B) Line 2 and C) Line 3 on the north-facing slope. The trees on Line 1 represent ponderosa pine and the trees on Lines 2 and 3 represent lodgepole pine with the amount and spatial variation among the trees schematically representative of tree cover at the field site. There is also a rocky outcrop on Lines 1 and 2.....	20
Figure 2.6	Soil volumetric water content for the north-facing downslope sap flow plot (plot NF_Low) at 10 cm (A) and at 30 cm (B) and the south-facing downslope sap flow plot (plot SF_Low) at 10 cm (C) and at 30 cm (D).....	21
Figure A.1	Example of segyread output in the terminal window. Note that in this case, there is no sx term because $sx = 0$, but sx will be defined for any file where the source location is not equal to zero.....	39
Figure A.2	Example of the path to your .csv file with the stack input data and the path to the segy files using python.....	40
Figure A.3	Example of how to hard code geophone locations if they are placed at non-integer distances.....	40
Figure A.4	Example plots of the individual shots to be stacked at a single shot location using the stackData.py script.....	41
Figure A.5	Example script for manually fixing geophone spacing for those that are not at integer locations.....	43

Figure A.6	Example of the window where you pick the first arrival times of the stacked shots at each location.....	43
Figure B.1	Elevation profile and distance for seismic Line 1 on the south-facing slope generated by the <i>extractElevationProfile_rev2.py</i> script in Anaconda.....	47
Figure B.2	P-wave velocity profile, p-wave vertical velocity gradient, ray paths, and ray coverage for seismic Line 1 generated by the pyGIMLi inversion using the script <i>StreamLineInversion_Pwave.py</i>	48
Figure B.3	The residual (observed – modeled) as a function of the observed travel times, and modeled vs observed travel times for seismic Line 1.....	49
Figure B.4	The root mean square (RMS) misfit for each shot location for the p-wave inversions for Line 1.	49
Figure B.5	Elevation profile and distance for seismic Line 2 on the south-facing slope generated by the <i>extractElevationProfile_rev2.py</i> script in Anaconda.....	50
Figure B.6	P-wave velocity profile, p-wave vertical velocity gradient, ray paths, and ray coverage for seismic Line 2 generated by the pyGIMLi inversion using the script <i>StreamLineInversion_Pwave.py</i>	51
Figure B.7	The residual (observed – modeled) as a function of the observed travel times, and modeled vs observed travel times for seismic Line 2.....	52
Figure B.8	The root mean square (RMS) misfit for each shot location for the p-wave inversions for Line 2.....	52
Figure B.9	Elevation profile and distance for seismic Line 3 on the south-facing slope generated by the <i>extractElevationProfile_rev2.py</i> script in Anaconda.....	53
Figure B.10	P-wave velocity profile, p-wave vertical velocity gradient, ray paths, and ray coverage for seismic Line 3 generated by the pyGIMLi inversion using the script <i>StreamLineInversion_Pwave.py</i>	54
Figure B.11	The residual (observed – modeled) as a function of the observed travel times, and modeled vs observed travel times for seismic Line 3.....	55
Figure B.12	The root mean square (RMS) misfit for each shot location for the p-wave inversions for Line 3.....	55
Figure B.13	Hourly sap flow velocities in cm/hr from June to September of 2021 for all four sap flow plots, two on the south-facing slope A) SF_High and B) SF_Low and two on the north-facing slope C) NF_High and D) NF_Low. The gray lines are the sap flow velocities for each individual tree and the black lines are the average of all trees at each plot.....	56
Figure B.14	Hourly sap flow velocity in cm/hr from June to September of 2021 for A) Tree #5 and B) Tree #6 from the NF Low plot or North-Facing Downslope	

plot. These two trees display slight trends from June-September however as the sap flow data from the rest of the trees at this plot are very noisy, it is difficult to generate meaningful conclusions from just two trees. They have been included here for reference and further study is needed to gather more viable data.....57

Figure B.15 Spectrograms sap flow plots A) SF High, B) SF Low, C) NF High, and D) NF Low. These plots display the estimated short-term, time-localized content of the provided data. Normalized frequency is on the y axis, time is on the x axis, and the colorbar indicates frequency intensity. There is no consistent change in dominant frequency with time here, perhaps because sap flow data are always dominated by a diel signal. That said, there is some different in power with time and between hillslopes that might be interesting for future analysis.....58

LIST OF TABLES

Table 2.1 Plot ID and location, number of trees installed with sensors, number of sensors used out of the 8 installed (given installation issues) and type of tree instrumented with sensors at each plot.....14

Table A.1 Additional example of how to set up a stack input guide. From left to right there is the shot location (-20, -10, 0, etc.), the “3”, and the file numbers of the shots we want to stack at the given shot location (3000, 3001 etc.)38

LIST OF EQUATIONS

EQ 2.1 Gauss-Newton Inversion Equation.....16

ACKNOWLEDGEMENTS

First and foremost, I would like to thank my advisor, Dr. Kamini Singha. Her support and guidance throughout this project have been invaluable. I am grateful for the opportunity she provided me to undertake this project and for her continuous encouragement to push myself and grow both technically and academically. Thank you to my co-authors Joel Singley, Nicole Hornslein, Jeff Shragge, and Holly Barnard for their invaluable feedback and ongoing guidance throughout the course of this project. Their contributions have significantly enhanced the quality of my work. I would like to extend my appreciation to my committee members Jeff Shragge and Alexis Sitchler for their unique perspectives and valuable contributions to this project. Thank you to all the professors, faculty, and fellow students at Mines who have generously shared their technical and professional expertise with me. Their contributions have not only enriched my academic growth but have also helped me grow as an individual. A special thank you to everyone in the lab for being an instant support network both in terms of research and coursework. It has been a privilege to share this journey with you all. Lastly, I would like to express my deepest gratitude for my family, partner, and friends, without whom I would not be here, for their unwavering encouragement, support, and humor throughout my time at Mines.

CHAPTER 1

GENERAL INTRODUCTION

Trees are essential to ecosystems and human life. They help to mitigate climate change by absorbing carbon dioxide, acting as natural carbon sinks, and reducing the negative effects of greenhouse gases. Not only do trees play a vital role in ecosystems, but they are also an essential resource for infrastructure and have immense societal value, providing shade and reducing urban heat island effects, and helping to improve air quality and prevent erosion (Akbari et al., 2001; Pramova et al., 2012). As climate change progresses, the severity of weather events such as drought is expected to increase and negatively affect belowground water storage and thus the tree communities and ecosystems reliant on this water supply to survive (Bales and Dietrich, 2020; Pokhrel et al., 2021). Belowground water storage not only maintains tree communities, but also entire stream and river systems essential for water supply and urban and agricultural uses (Bales and Dietrich, 2020).

Research has shown that water storage within the critical zone—the layer of earth from atmosphere through groundwater that humans depend on—is correlated to distinct plant communities and the underlying lithology. As climate change alters the water cycle, it is expected that there will be changes in groundwater storage and supply that could be irreversible. Due to the importance of trees and belowground water storage not only to each other but to society and broader ecosystems, it is essential that we explore how to better characterize these systems as they respond to a changing climate.

The focus of this study is quantifying the potential effects of subsurface heterogeneity on sap flow in trees and exploring the efficacy of two methods—seismic refraction and sap flow—to characterize this relationship. Sap flow can be used as a proxy for quantifying tree

productivity and is used to estimate water usage and transpiration in trees (Sun et al., 2021).

Higher sap flow velocities typically indicate that a tree is using more water for transpiration and is thus more productive (Giménez et al., 2013). Water within plants influences plant growth, thus growth is impacted in the absence of adequate water (Giménez et al., 2013). Seismic refraction is useful for characterizing the interfaces between subsurface layers and providing information about the porosity of these layers, which influences their water-holding capacity (Klos et al., 2018; Flinchum et al., 2022). The integrated analysis of seismic imaging and sap flow data is underutilized in investigating links between tree productivity and subsurface water-storage patterns. Here, we look to explore how these two methods, used in unison, may allow us to build relations between what we see above ground and what is below our feet.

CHAPTER 2

SEISMIC REFRACTION TO EXPLORE THE INFLUENCE OF BELOWGROUND WATER STORAGE ON SAP FLOW VELOCITIES IN PINES

2.1 Abstract

Water storage in the critical zone acts as a buffer between trees and the effects of climate change by aiding in a tree community's ability to survive water scarcity. Consequently, predicting how subsurface water-storage patterns may change under a changing climate and how trees will respond to these changes is vital for accurately assessing tree mortality. Here, we conducted a study on two opposing slopes of Gordon Gulch in the Boulder Creek Critical Zone in Boulder, CO. Sap flow—which is used as a measure of tree productivity—and seismic refraction data were collected to explore how and if subsurface water storage is related to the productivity of ponderosa and lodgepole pine trees. Four sap flow plots, two on north-facing and two on south-facing slopes, each containing roughly 8 trees, were instrumented with sap flow sensors. There is a greater depth of saprolite and unconsolidated material on the north-facing slope of Gordon Gulch, where we see an abundance of tightly spaced lodgepole pine trees. The depth of the saprolite and unconsolidated layers on the south-facing slope are shallow in comparison to the north-facing slope with the south-facing slope consisting of sparsely spaced ponderosa pine trees. Three out of the four sap flow plots displayed seasonal trends with sap flow velocity values that appear to generally correspond to subsurface water storage capacity between sites on each slope, although it was clear other variables also controlled sap flow. Sap flow velocities differed between the two plots on the south-facing slope, which had the same tree species on them, indicating that differences in the thickness of water-holding materials and other environmental and biological factors, such as slope/aspect and rooting depth, likely influence sap

flow differently between sites. Sap flow velocities decreased significantly following August for the south-facing upslope plot while they remained high for the downslope plot, leading us to speculate that belowground water storage potential might be positively influencing sap flow rates into late summer. In short, we found that differences in water storage capacity may influence sap flow velocities but are convolved with other factors such as solar radiation, soil/rock moisture, and rooting depth.

2.2 Introduction

Quantifying the relationship between tree health and subsurface water storage is important for predicting scenarios where trees may experience drought-based mortality (e.g., Flinchum et al., 2018; Klose et al., 2018; Hahm et al., 2019;). Recent research has shown that the availability of subsurface water is crucial for plant resilience against drought, and that subsurface water storage capacity can be correlated to distinct plant communities (e.g., Bales et al., 2020; McCormick et al., 2021; Hahm et al., 2019, 2022). The distribution of plant communities throughout ecosystems is commonly attributed not only to subsurface water storage, but also to landscape, ecosystem and ecological processes, anthropogenic activities, and climatic controls (Aguiar & Sala, 1994; Richardson et al., 2007; Punyasena et al. 2008; Dawson et al., 2020). In recent years, several studies have closely investigated links between subsurface water storage and plant communities in terms of how subsurface structure affects plant communities' ability to survive the increasing severity and frequency of droughts (Bales and Dietrich, 2020, Rempe et al., 2020).

Geology controls potential water storage within the critical zone (Riebe et al., 2017; Flinchum et al., 2018; Klos et al., 2018; Bales and Dietrich, 2020), which is defined as the area

of the Earth from the bottom of the groundwater to the upper limits of vegetation (National Research Council [NRC], 2001; Brantley et al., 2007). Weathered bedrock allows for water to be stored for extended use by trees and other organisms, and this water storage can act as a buffer between plants and the effects of climate change (Graham et al., 2009; Riebe et al., 2017; Bales and Dietrich, 2020, Rempe et al., 2020). There has been increasing awareness that many tree species rely on this groundwater as a reservoir to survive adverse conditions (Goulden and Bales, 2019; McCormick et al., 2021; Hahm et al., 2022). For example, Bales and Dietrich (2020) found that there were regional differences in tree mortality rates in response to a severe multiyear drought controlled by belowground water storage, and that a lack of subsurface water storage can be linked to increased tree mortality. In this case, over 150 million trees died in California due to limited belowground water storage and high-density forests. Similarly, Hahm et al. (2019) discovered that variations in the weathering of the underlying bedrock contributed to the variation in plant communities in regions with similar temperature and precipitation regimes.

Changes in water storage throughout the critical zone are inevitable with climate change, and with these changes, trees have the potential to be more susceptible to drought (Goulden and Bales, 2019; Bales and Dietrich, 2020; IPCC, 2021; Hahm et al., 2022). With increasingly severe floods, droughts, wildfires, and weather, quantifying changes in groundwater distribution and storage is important to predicting how the health of forest populations will change, and how trees may evolve to survive in future water-limited, semi-arid environments (D'Odorico et al., 2007; Klos et al., 2018; Hahm et al., 2019; Bales and Dietrich, 2020). Previous studies have estimated landscape and tree resilience, where resilience is defined as the trees' ability to survive and recover from extended droughts, using a variety of methods such as remotely sensed satellite data, GIS techniques, soil data, visual observations, and physical measurements (Debeljak et al.,

2009; Johnstone et al., 2010; Verbesselt et al., 2016; Poorter et al., 2016). These techniques have proven to be helpful; however, until recently, few studies have considered subsurface water storage patterns when generating resiliency maps over broad spatial scales.

Geophysical methods offer one means to explore the deep critical zone and they are increasingly being used to gather data over larger and deeper spatial scales (Parsekian et al., 2015; Befus et al., 2011; Flinchum et al., 2018). For example, seismic refraction and electrical resistivity have been used to quantify variations in regolith porosity and to discern how water storage varies across a landscape (Holbrook et al., 2014). While geophysical methods have been frequently used to map subsurface structure or changes in moisture in the critical zone, there has been more limited work exploring the connections between the subsurface and tree productivity. The use of geophysical methods in conjunction with more standard measurements of ecohydrological processes such as transpiration and precipitation or remote sensing of vegetation properties have been explored largely in the past few years (Klos et al., 2018; Hahm et al., 2019; Goulden and Bales 2019; Bales and Dietrich, 2020). However, none of this research connected subsurface data from seismic refraction to tree productivity as defined by sap flow rates.

Sap flow within xylem sapwood tissue is often used to estimate a tree's water usage and transpiration (Sun et al., 2021). The velocity of ascending sap within a tree can be used as an indicator that the tree is using water for transpiration where higher velocities typically suggest greater productivity (Giménez et al., 2013). Water is a primary driver in plant growth and affects most physiological processes within plants, thus quantifying both the water available to trees and their ability to use this water for transpiration is essential for quantifying the productivity and health of the trees (Giménez et al., 2013).

Here, we use seismic refraction and sap flow sensors to quantify how water storage potential in the critical zone affects tree productivity in a semi-arid catchment in the Front Range of Colorado. Many environmental factors influence tree growth and sap flow including soil moisture, slope and aspect, topographic position, and subsurface water storage capacity (Adams et al., 2014; Bales and Dietrich, 2020). This study consists of two research objectives:

- 1) To connect the sap flow within two tree species, *Pinus ponderosa* (ponderosa pine) and *Pinus contorta* (lodgepole pine), to critical zone architecture on north- and south-facing slopes to determine how and if subsurface heterogeneity influences sap flow velocities, and
- 2) To explore how seismic refraction and sap flow be utilized effectively together to draw meaningful conclusions about how subsurface heterogeneity impacts sap flow velocities.

Quantifying the relationship between subsurface moisture and critical zone structure using sap flow and seismic methods could provide insight into how subsurface structure controls tree and/or ecosystem productivity and vulnerability, and therefore development of resilience maps.

2.3 Site Description

This study was conducted in the Gordon Gulch watershed (Figure 2.1), a semi-arid catchment on the Front Range of the Rocky Mountains, 20 miles west of Boulder, Colorado. Gordon Gulch is located within the Arapaho National Forest and covers an area of roughly 2.6 km² with an average elevation of 2600m (Diek et al., 2014). Additionally, it is underlain primarily by Precambrian biotite gneiss, with sparse outcrops of Precambrian granite and Precambrian quartz monzonite (Buraas, 2009; Diek et al., 2014).

The Gordon Gulch watershed has been the focus of multiple projects examining various pine tree communities and some investigating subsurface structure and hydrologic processes

(Leopold et al., 2013; Christensen et al., 2020; Adams et al., 2014; Befus et al., 2011). Gordon Gulch has a history of mining exploration and is currently a site of diverse recreational, residential, and scientific activities (Lovering and Tweto, 1953)

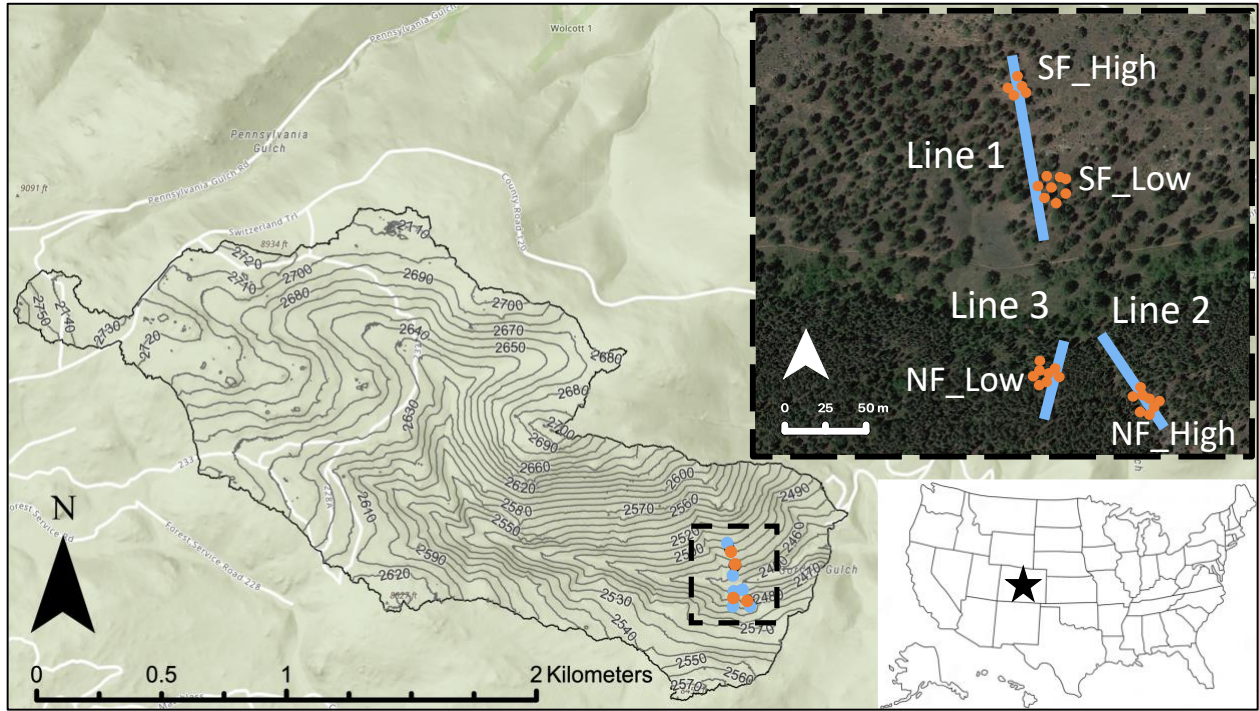


Figure 2.1 Map of the Gordon Gulch watershed with the field site outlined in a black dotted line, highlighting the location of our three seismic lines and four sap flow plots. The three seismic lines are labeled Lines 1, 2, & 3 (in blue), and the four sap flow plots are labeled SF_High, SF_Low, NF_High, NF_Low, with the green dots indicating the locations of the individual trees installed with sap flow sensors. Soil moisture probes were installed centrally at each of the sap flow plots.

The valley of Gordon Gulch is east-west oriented resulting in stark differences between the north and south facing aspects (Diek et al., 2014). The valley is also largely forested with the forests on the north-facing slopes being generally more vegetated compared to the south-facing slopes (Figure 2.1), with the north-facing slopes consisting primarily of lodgepole pine, a shallow rooted tree, and the south-facing slopes consisting primarily of ponderosa pine, a deeply rooted tree (Diek et al., 2014; Burns and Barbara, 1990; Noble, 1979). Anderson et al. (2021)

found that during the midwinter, the south-facing slopes of Gordon Gulch receive roughly 2-3 times more solar radiation than the north-facing slope, and that the lodgepole forests dominating that slope, provide more shade than the ponderosa forests on the south-facing slope. The north-facing slopes have a higher wetness compared to the south-facing slopes and develops snowpack each winter resulting in persistent snowmelt while the south-facing slopes have patchy and inconsistent snow cover resulting in intermittent snowmelt (Diek et al., 2014; Hinckley et al., 2014). The increased wetness and weathering on the north-facing slopes have resulted in greater saprolite and soil thicknesses (Diek et al., 2014). Additionally, from 2012-2019 the yearly average depth of the water table in the upper part of the Gordon Gulch is noted as ~9 m on the north-facing slope and ~6 m on the south-facing slope (Salberg et al., 2022). While the differences in tree species and cover are likely attributed to differences in snow cover and solar radiation, differences in sap flow within each slope may be influenced by the variations seen in the different weathering patterns and thus water-holding capacity seen in seismic data with slope (Bandler, 2016, Befus et al., 2011), although some seismic data shows weathering patterns with little changes with slope aspect as well (St. Clair et al., 2015).

Three seismic lines were chosen given differences in tree type between the opposing slopes (Figure 2.1). The two north-facing slope lines were chosen for difference in tree density and ground cover; the spacing of the lodgepole pine trees alone Line 2 was less dense than those alone Line 3, and the ground cover at Line 2 included various shrubs and some rock outcrops while Line 3 crossed many fallen trees and low ground cover. Two sap flow plots were on each slope including an upslope and downslope site, with the two locations on the north-facing slope chosen for differences in the tree cover of the lodgepole pine trees and varying ground cover as noted above (Figure 2.1). Four sap flow plot locations were chosen for variation in tree type,

density, and aspect with one high and one low plot on both the north and south facing slopes (Figure 2.1). The area surrounding Plot NF_High (Figure 2.1, 2.2) was largely open with rock outcrops and sparse ground cover, whereas the area surrounding Plot NF_Low (Figure 2.1, 2.2) consisted of densely packed trees, abundant ground cover, and fallen trees. Plots SF_High and SF_Low (Figure 2.1) are somewhat similar with more understory and more dispersed tree cover, but Plot SF_Low is just below a rocky outcrop (Figure 2.3) and Plot SF_High is more exposed (Figure 2.3).



Figure 2.2 Images of the area near sap flow Plots A) NF_High and B) NF_Low on the north-facing slope of Gordon Gulch.



Figure 2.3 Images of the area near sap flow Plots A) SF_High and B) SF_Low on the south-facing slope of Gordon Gulch.

2.4 Methods

2.4.1 Sap Flow Collection Methods

Sap flow data were collected hourly via sap flow sensors at four plots in Lower Gordon Gulch, two on the south-facing slope noted as SF_High (lower density ponderosa) and SF_Low (dense ponderosa) and two on the north-facing slope noted as Plot NF_High (dense lodgepole and limber pine) Plot NF_Low (dense lodgepole). SF_High and NF_High are both upslope plots and SF_Low and NF_Low are both downslope plots (Figure 2.1).

Eight sap flow sensors were installed at each site (Table 2.1). Sap flow Plots SF_Low, NF_High, and NF_Low all had a single sap flow sensor per tree, however Plot SF_High had multiple sap flow sensors in a few of the trees. Sap flow Plots SF_High and SF_Low consisted of only ponderosa pines, Plot NF_High consisted of only lodgepole pines, and plot NF_Low consisted of four limber pines and four lodgepole pines, all instrumented with sap flow sensors. Each tree was installed with an inner and outer sap flow sensor to measure the velocity of sap flow at 1 cm and 2.5 cm within the sapwood. The inner and outer sensors for each tree were then averaged to estimate the average sap flow or xylem water flux after being checked individually to ensure seasonal trends were present indicating that the sensors were installed correctly within the sapwood. Four sap flow sensors were discarded from the north-facing upslope Plots NF_High (Table 2.1) and three were discarded from the south-facing upslope Plot SF_High (Table 2.1) as they were missing too many data to be effectively analyzed.

Table 2.1 Plot ID and location, number of trees installed with sensors, number of sensors used out of the 8 installed (given installation issues) and type of tree instrumented with sensors at each plot.

Plot ID	Location	Number of trees with sensors	Number of sensors used	Tree type
SF_High	south-facing upslope	5	5	ponderosa pine
SF_Low	south-facing downslope	8	8	ponderosa pine
NF_High	north-facing upslope	8	4	lodgepole pine & limber pine
NF_Low	north-facing downslope	8	8	lodgepole pine

Our sap flow sensors were built utilizing the compensation heat-pulse method, which has a heating element inserted between two temperature sensors, and measures the time taken for the heat pulse to travel to the temperature sensors from the heating element to determine the velocity of the heat pulse and thus the sap flow (Burgess et al., 2001). The four plots were installed in June of 2021 and the raw data from the 2021 growing season were downloaded in December of 2021 as the trees entered the dormant season. Sap flow sensors were connected to a datalogger and multiplexer (CR1000X and AM16/32b; Campbell Scientific, Logan UT, USA) and data were collected at 15-minute intervals at each plot. The data acquired from the lodgepole pines were processed using an allometric relation to estimate sapwood area from bole area detailed in Mitra et al. (2019) and the data acquired from the ponderosa pines were processed using methods from Long and Dean (1986) to estimate sapwood area.

2.4.2 Seismic Refraction Survey Methods

Shallow seismic refraction surveys were also conducted at three locations in Gordon Gulch, including one transect on the south-facing slope and two on the north-facing slope (Figure 2.1). The survey lines were also chosen to intercept the sap flow plots, with survey Line 1 running through Plot SF_High (lower density ponderosa) and Plot SF_Low (higher density ponderosa) on the south-facing slope, and Lines 2 and 3 running through Plots NF_High (high density lodgepole and limber) and NF_Low (high density lodgepole), respectively, on the north-facing slope (Figure 2.1).

Data were collected using a 96-channel cabled Geometrics Geode Exploration Seismograph with 48 14.5-Hz vertical component geophones. Line 1 on the south-facing slope was ~172.5 m long with a geophone spacing of 2.5m (Figure 2.1). Lines 2 and 3, both collected on the north-facing slope, were ~100.5 m and 67 m with a geophone spacing of 1.5 and 1 m, respectively (Figure 2.1). The seismic source was produced via a 5-kg sledgehammer striking a 15-kg steel plate against the surface of the ground. Five hammer strikes were taken at designated shot locations along each line and stacked to enhance the amplitude of the seismic signal and minimize noise. Off-end shots were taken up to 45 m on either side of Line 1, 30 m on either side of Line 2, and 20 m on either side of Line 3. Data on all lines were collected at a 0.5 ms sampling rate with a 1 s record length. The arrival times for the seismic surveys were picked manually after the shots were stacked, and no pick was made in cases where the first arrival was noisy to minimize error.

The seismic data was processed and inverted using the Python Geophysical Inversion Modeling Library (pyGIMLi) (<https://www.pygimli.org/>), an open-source library used for the modeling and inversion of geophysical data (Rucker et al., 2017). For this project, PyGIMLi was

used through Spyder, an open-source scientific environment that utilizes python. The original .dat files were converted to .segy files, stacked, picked, and then inverted given elevation data. PyGIMLi models seismic energy as rays using a shortest-path algorithm, which calculates a ray path and allows for cells to only be populated in the model if a ray path passes through them (Dijkstra, 1959; Moser, 1991; Moser et al., 1992; Flinchum et al., 2022). PyGIMLi also generates a triangular mesh and indexes the locations of each electrode/geophone as a position within this mesh. PyGIMLi utilizes a generalized and deterministic Gauss-Newton inversion (Equation 2.1) with flexible regularization (Gance et al., 2012; Rucker et al., 2017):

$$\Omega = \|W_d(F(m) - d)\|_2^2 + \lambda \|W_m(m - m_0)\|_2^2 \quad (2.1)$$

where Ω is the objective function we seek to minimize, W_d is the data weighting matrix containing the reciprocal of the data errors, W_m is model constraint matrix, $F(m)$ is a forward operator or forward response, m is a discrete parameter distribution, d is model parameters to the data vector, m_0 is a reference model, λ is a dimensionless factor that scales the influence of the regularization term (Rucker et al., 2017).

The seismic refraction surveys show three subsurface layers as defined by Flinchum et al. (2018): soil and saprolite, the latter of which is defined by extensively friable and weathered rock while still retaining structure, with p-wave velocities from ~100-1200 m/s; 2) weathered bedrock, characterized by fracturing due to chemical and physical weathering, with p-wave velocities ranging from 1200-4000 m/s; and 3) protolith, characterized as bedrock with minimal chemical and physical weathering and p-wave velocities of 4000 m/s and greater. Saprolite and soil are considered together because the seismic survey is not able to resolve clearly between the two. The depth and thickness of the layers were estimated qualitatively based on the inversion

images and each of the layer types vary in depth, thickness, and structure between the three seismic surveys.

2.4.3 Soil Moisture Methods

Soil volumetric water content was collected on two sensors at 15-minute intervals at 10 and 30 cm depths located centrally at each of the four sap flow sites using Stevens HydraProbes (Figure 2.1).

2.5 Results

2.5.1 Sap Flow Results

Differences in sap flow are notable with slope aspect. South-facing plots SF_High and SF_Low have values up to 13.6 cm/hr compared to the north-facing slopes NF_High and NF_Low which had values up to 9.2 cm/hr (Figure 2.4). The sap flow data for north-slope plots SF_High and SF_Low display diurnal fluctuations seasonally, and generally decrease in maximum sap velocity from June to September (Figure 2.4A, B). The sap flow data for Plot NF_High also displays diurnal fluctuations seasonally; however, these data have lower sap flow velocities than sites SF_High and SF_Low and less distinct seasonal trends (Figure 2.4). The sap flow sensors at Plot NF_Low were likely installed within the heartwood and did not display the same diurnal or seasonal patterns as the other three plots thus it has not been included here. Sap flow velocities for Plot NF_Low can be found in Appendix B. Sap flow from two of the trees at the NF_Low plot have also been included in Appendix B as they displayed slight seasonal trends, however the lack of viable data at this site limits our ability to meaningfully include them in our interpretation.

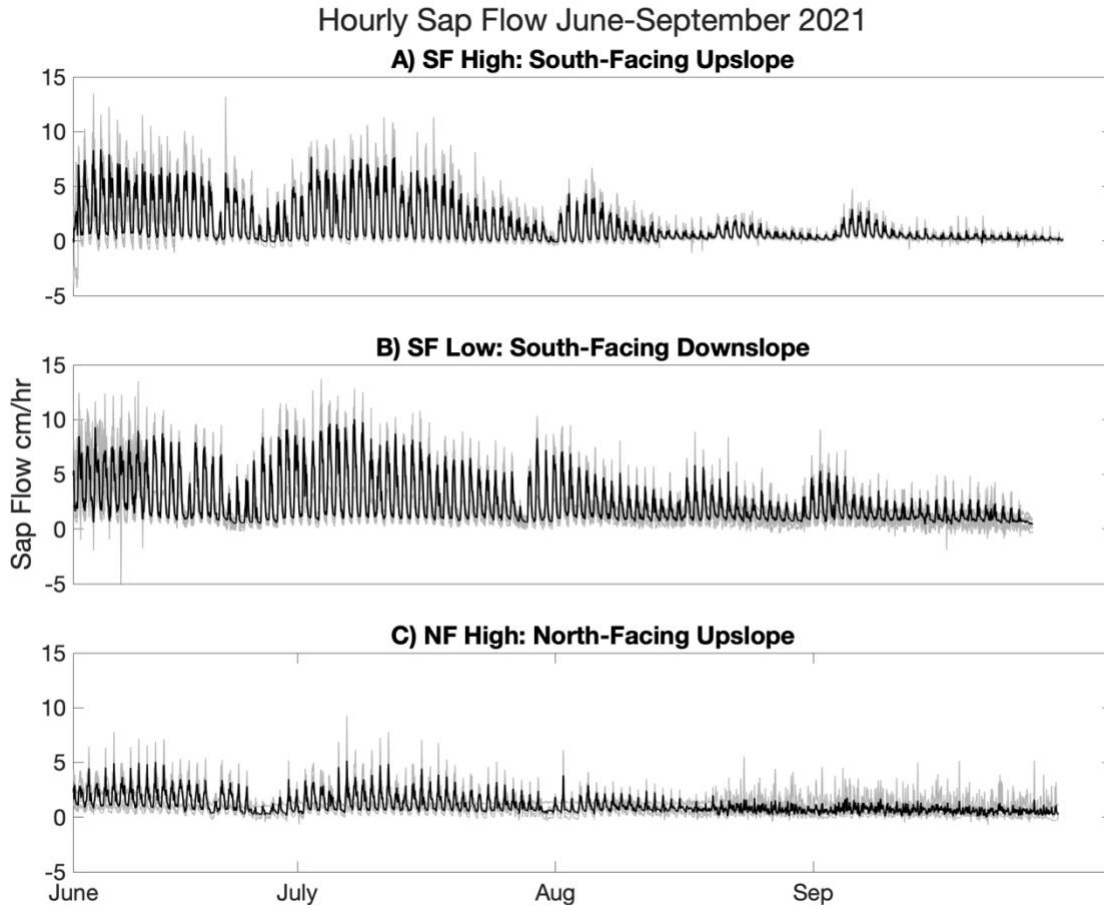


Figure 2.4 Sap flow velocities in cm/hr for plots (A) SF_High and (B) SF_Low on the south-facing slope and (C) NF_High on the north-facing slope from June-September 2021. The gray lines are sap flow collected for each tree at each plot and the black lines are the average sap flow velocities of all individual trees at each plot.

2.5.2 Seismic Results

There are notable subsurface differences in layer thickness between slope aspects. The thickness of the soil/saprolite layer for Line 1, which goes through sap flow Plots SF_High and SF_Low on the south-facing slope, ranges from about 2-6 m, getting thinner in the middle of the line where an outcrop appears at the surface, just above Plot SF_Low, and thicker towards both ends of the survey line (Figure 2.5A). The thickness of the saprolite layer does not appear

appreciably different between Plots SF_High and SF_Low. The thickest area of soil/saprolite at Plots SF_High and SF_Low along Line 1 are roughly the same at ~13 m. SF_Low has a thinner soil/saprolite layer thickness of 10 m compared to SF_High at 12 m. While the soil/saprolite at SF_High is overall slightly thicker, the soil/saprolite at SF_Low has a greater range of thickness. Notably, Plot SF_Low is located just below the outcrop where the saprolite layer is thinnest along the line. Lines 2 and 3, which go through sap flow Plots NF_High and NF_Low, respectively, on the north-facing slope, have slightly thicker saprolite layers ranging from ~2-12 m (Figure 2.5B, C). In terms of the weathered bedrock, it is thinnest along Line 1 at roughly 10 m thick and gets thinner towards the middle of the line, similar to the overlying soil and saprolite, and thicker towards the ends (Figure 2.5A). Line 2 has the thickest weathered bedrock layer, which is 10-20 m thick at the beginning of the line. This layer thins near an outcrop visible at the surface around 45 m along the line (Figure 2.5B). Line 3 has a 10-15 m thick layer of weathered bedrock, but with no visible outcrop on the surface (Figure 2.5C). Lastly, the protolith layer begins at a depth of roughly 10 m for Line 1, but deeper for Line 2 and Line 3 (Figure 2.5). There is a section of protolith jutting up into the fractured bedrock approximately 40-50 m from the start of Line 2 about 10 m under the surface corresponding roughly to the outcrop at the surface (Figure 2.5B)

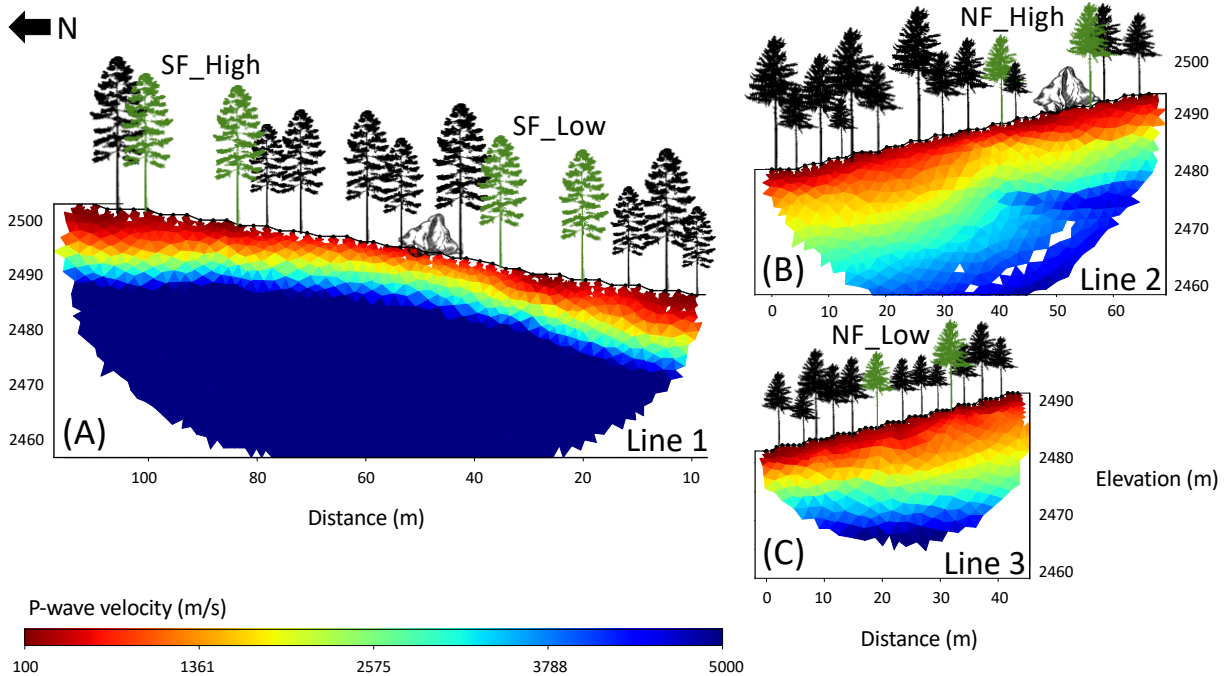


Figure 2.5 P-wave velocities for the three seismic lines with the start and end of the sap flow plots shown as green trees. A) Line 1 on the south-facing slope and B) Line 2 and C) Line 3 on the north-facing slope. The trees on Line 1 represent ponderosa pine and the trees on Lines 2 and 3 represent lodgepole pine with the amount and spatial variation among the trees schematically representative of tree cover at the field site. There is also a rocky outcrop on Lines 1 and 2.

2.5.3 Soil Moisture Results

The soil VWC at all locations show seasonal trends, with a large spike in June corresponding to spring snowmelt. There are differences with slope, however; the soil volumetric water content (VWC) on the lower north-facing slope at sap flow Plot NF_Low (Figure 2.6A), which receives less solar radiation, is greater at 10 cm with a peak value of 0.32 compared to the lower south-facing slope at sap flow Plot SF_Low (Figure 2.6B) at 10 cm with a peak value of 0.16. The soil VWC at 30 cm is more similar between the lower north-facing and south-facing slopes with the peak values of 0.18 and 0.16 respectively. The soil VWC was found to be significantly different between the north-facing and south-facing locations at both 10 and 30 cm

based on an Ansari-Bradley test of variance with p- values of 0.0086 and 1.9e-11 for each location respectively, and the Wilcoxon rank-sum test, with p-value of 0 for both locations.

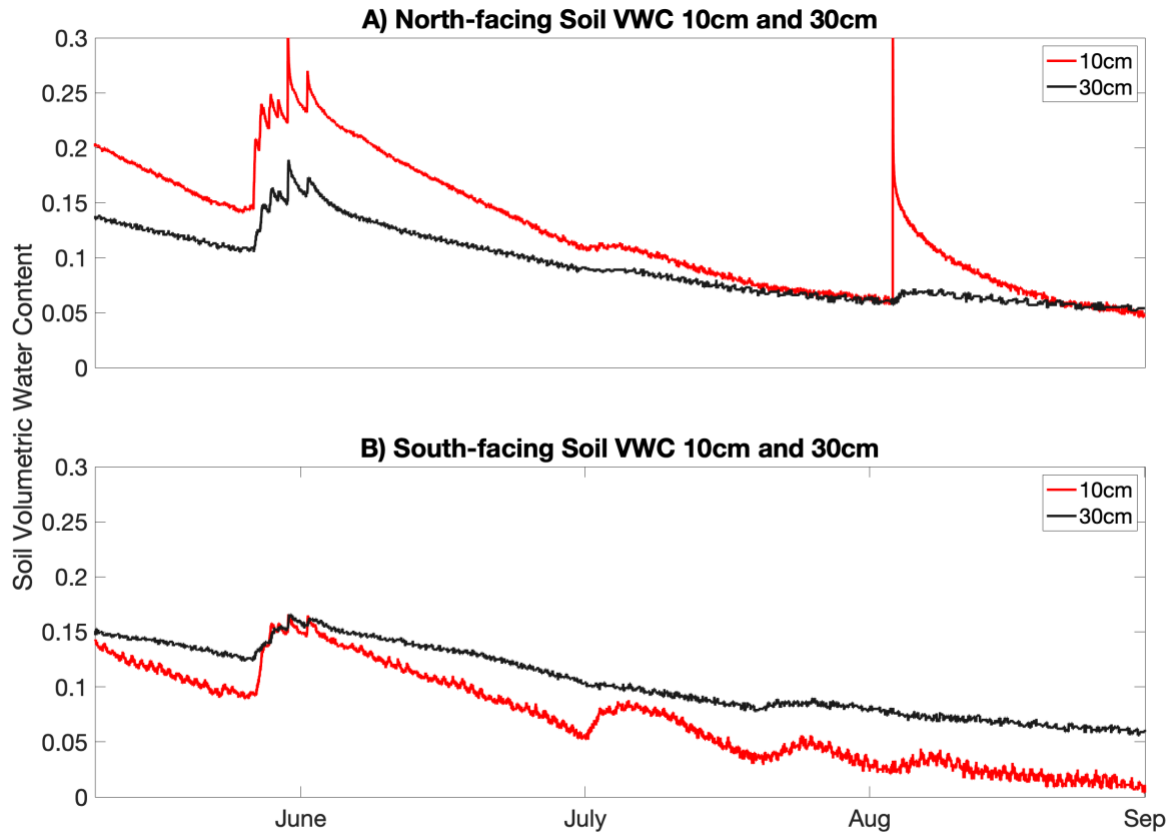


Figure 2.6 A) Soil volumetric water content (VWC) for the north-facing downslope sap flow plot (Plot NF_Low) at 10 cm and at 30 cm and B) the south-facing downslope sap flow plot (Plot SF_Low) at 10 cm and at 30 cm. The soil VWC at 10 cm is in red and at 30 cm is in black for the north/south-facing slopes.

2.6 Discussion

There are distinct differences in sap flow velocities between the north-facing and south-facing slopes which are expected given differences in insolation and species. The sap flow velocities collected from south-facing Plots SF_High and SF_Low, which are measured on ponderosa pine, have higher values than those from the north-facing plots, which were primarily

lodgepole and limber pine. The limber pines instrumented at Plot NF_High were found to have similar values and trends to the lodgepole pines at this plot. Empirical evidence suggests that lodgepole pine can have lower sap flow rates than ponderosa pine (Burns, 2022) and is a more shallowly rooted tree (Burns and Barbara, 1990; Noble, 1979). The north-facing generally has a shallower water table than the south-facing slope which could influence tree distribution between slopes and water availability. Also, the conducting area of lodgepole pine can be thin enough that the inner sap flow sensor will be in the heartwood, which is non-conducting.

Besides species composition, solar radiation is undoubtedly a control on sap flow. South-facing Plots SF_High and SF_Low are notably more open than south-facing Plots NF_High and NF_Low, with sparse underbrush, little shade, and multiple rock outcrops. On the north-facing slope alone, Plot NF_High is more open compared to the area surrounding Plot NF_Low, which is littered with fallen trees and consists of a dense tree spacing. The south-facing slope receives a greater amount of solar radiation compared to the north-facing slope (Anderson et al., 2021) and has different density and species of vegetation, which undoubtedly influences soil moisture differences between the two slopes. The lack of shading from the ponderosa pines on the south-facing slope likely contributes to increased solar radiation along with the aspect of the slope, which could drive transpiration. As noted above, the south-facing slope also exhibits more sparse tree cover, potentially leading to less competition for light and water resources. Thus, differences in subsurface structure may not be the primary control on sap flow on the north-facing slope but may influence tree distribution. Although the saprolite and weathered bedrock layers are thinner on the south-facing slope (Line 1) compared to the north-facing slope (Lines 2 and 3), the sap flow values from the south-facing slope are higher, indicating that species differences are likely the primary driver in sap flow rates.

Within slopes we also see some interesting differences in sap flow. Sap flow velocities between Plots SF_High and SF_Low were found to be significantly different from each other. The variance in sap flow velocities between Plots SF_High and SF_Low were found to be significantly different via an Ansari-Bradley test of variance with a p value of $1.8e-156$, and the medians were found to be significantly different via the Wilcoxon rank-sum test with a p value of $1.3e-235$. Overall, Plot SF_Low exhibits greater sap flow rates than Plot SF_High, with values at Plot SF_Low from August-September peaking up to roughly 8 cm/hr while values at Plot SF_High from August-September peak at roughly 4 cm/hr. This leads us to hypothesize that the subsurface heterogeneity might influence sap flow velocities given a somewhat similar density of trees and tree species. Plot SF_Low is farther downslope where a slightly thicker layer of topsoil and saprolite exists in some areas indicating the potential for increased subsurface moisture. The soil at Plot SF_Low was also less rocky than at Plot SF_High, with augering possible down to 20-30 cm versus less than 10 cm at Plot SF_High. Plot SF_Low is also located right below an outcrop where the soil and saprolite layers are the thinnest along line 1. This could influence both the movement and storage of subsurface moisture and could lead to increased rock moisture just below this outcrop due to increased runoff.

It is difficult to meaningfully parse differences in sap flow at our selected sites given the convolution of differences in species type, soil moisture, regolith thickness, and solar radiation. Trees in areas with ample access to water storage on the north-facing slope tended to have lower sap flow velocities as a function of tree density and decreased solar radiation. This has implications for the resilience of tree communities that have access to ample subsurface water storage but are limited by environmental factors like solar radiation. Areas with higher belowground water storage but limited solar radiation likely would not benefit from the same

forest management techniques as an area where the trees are limited by their access to subsurface moisture and thus void of a potentially crucial reservoir in the case of extreme drought.

Ultimately it is likely that subsurface structure and water storage potential can aid in trees surviving extreme weather events and that a lack of subsurface water storage jeopardizes tree communities' ability to survive.

We also note that the sap flow velocities decrease significantly following August for Plot SF_High while they remain high at Plot SF_Low throughout August and into September indicating that subsurface water storage capacity might be positively influencing sap flow rates into the late summer and early fall despite decreased solar radiation and precipitation. It is plausible that sap flow velocities at Plot SF_High are able to remain higher throughout August-September due differences in soil composition and soil and saprolite layering. Differences in sap flow between Plots SF_High and SF_Low could also be due to rooting depths and the depth of the soil moisture and water table where the trees at Plot SF_High must root more deeply to access belowground moisture while trees at Plot SF_Low do not need to go as far to access water. Conversely, as soil moisture decreases throughout the summer, there might be increased rock moisture stored around Plot SF_Low compared to the area around SF_High, thus the trees at Plot SF_Low are able to utilize this reserve of rock moisture to maintain higher peak sap flow velocities into the late summer and early fall. Differences in the water table depth between slopes might also influence sap flow leading not only to differences in tree distribution but also possible differences in sap flow. Slope likely influences soil and rock moisture as well where the trees at Plot SF_High are higher, more exposed, and available snowmelt would likely run down the slope and have a greater chance of pooling at Plot SF_Low. Plot SF_Low also being right below an outcrop could mean that precipitation is more likely to runoff this outcrop down to the area

surrounding Plot SF_Low as the saprolite and weathered bedrock layers coinciding with the aboveground outcrop are thinner compared to just below the outcrop at Plot SF_Low indicating a possible lack of water storage capacity in the near vicinity of the outcrop and a greater water storage capacity just below the outcrop at Plot SF_Low.

2.7 Conclusions

Investigating differences in tree type, tree cover, sap flow, and subsurface heterogeneity between slopes in Lower Gordon Gulch allowed us to explore the degree to which subsurface water-holding capacity influences sap flow rates between sites and on the same slope. Our seismic refraction surveys uncovered differences in the lithological interfaces between the north-facing and south-facing slopes, with the north-facing slope having thicker layers of weathered bedrock and saprolite thus likely a higher water storage potential compared to the south-facing slope. Slope dependent behavior has been seen at other sites, and this was not surprising given differences in the species present, but within-slope differences were difficult to parse with limited data. While we cannot draw concrete conclusions between the seismic data and the sap flow rates on the same slope, we do note that the thickness of the saprolite and weathered bedrock layers do not have a dominant influence on sap flow rates.

Sap flow rates differed between sites, and we attribute these differences to tree species, lithology, and environmental factors such as solar radiation and snowpack. Overall, ponderosa pines had greater sap flow rates than lodgepole pines, and the sap flow rates on the south-facing slope at Plot SF_High had lower velocities than Plot SF_Low despite having the same species present. Sap flow velocities at Plots SF_High and SF_Low both exhibit seasonal declines in max velocity; however, the trees at Plot SF_Low were able to sustain higher sap-flow velocities and

thus transpiration rates late into the summer despite a large decline in soil moisture. This result leads us to hypothesize that the trees at this location could be rooting deeper into the saprolite and weathered bedrock layers and utilizing the high moisture storage potential of this zone to sustain transpiration later into the summer. This result also leads us to hypothesize that slight differences in subsurface structure between these two plots influences sap flow rates, positively in the case of Plot SF_Low. Environmental variables confound easy interpretation of sap flow as a function of seismic velocity and further study is needed across broader spatial and temporal scales to accurately quantify how belowground water storage potential influences sap flow together with other environmental factors.

CHAPTER 3

FUTURE WORK

There is still work to be done at Gordon Gulch as well as other systems and locations to quantify the relationship more accurately between subsurface water storage and tree resilience, and future work is needed to draw concrete conclusions about how subsurface water storage availability might influence sap flow rates and how to better couple sap flow with seismic refraction methods. Here, I outline a few areas that might have improved this study that could be considered for future work. Better quantifying the relationship between trees and subsurface moisture across different environments should allow us to implement better forest management techniques and better predict where trees are at greater risk of mass die-off under a changing climate.

3.1 Increased Spatial Coverage

This project was restricted to a small sample of both seismic and sap flow data. While we were able to describe trends among the sap flow data, it is difficult to establish definite conclusions given only four sites, especially when one dataset was problematic. Our data show that sap flow velocities differ between slopes and tree species, and that there is variation amid each slope; however, we are left to speculate as to the degree of control that subsurface heterogeneity, among other environmental factors, has on these differences. For example, solar radiation likely influences sap flow between slopes; however, it is difficult to parse controls between solar radiation, sap flow, and subsurface moisture with limited datasets. Expanding data collection to other areas with both limited solar radiation and high belowground water storage potential to quantify sap flow trends and compare them to other locations would aid in deepening

the discussion surrounding what factors exert primary control over sap flow rates over a broader spatial scale. Furthermore, investigating areas for visual differences in tree cover and patterning among each slope and between slopes with aerial imaging before the installation of sap flow sensors would likely be advantageous in expanding the collection of sap flow data to areas with substantial or unusual differences that warrant further exploration.

The use of additional soil moisture probes both around individual trees instrumented with sap flow sensors and along the seismic lines could provide further information on the availability and variability of soil moisture through time as it might relate to changes in sap flow between individual trees and how differences in subsurface layering might influence the movement and volume of soil moisture between slopes.

3.2 Additional Methods

The coupling of seismic refraction and sap flow has seldom been the two standalone methods implemented in a project. Our goal was not only to compare differences in sap flow and subsurface heterogeneity between slopes, but also to explore the utility of seismic refraction and sap flow methods together. While the data collected and compared from each method illustrates potential trends between sap flow and the subsurface, the limited data set limits our ability to confirm more concrete conclusions. The addition of timelapse electrical resistivity imaging (ERI) to this study could prove a powerful partner to seismic refraction in allowing us to quantify subtle subsurface differences within the saprolite layers including the presence and spatial and temporal variability of water.

ERI has been shown to be useful in temporally imaging soil moisture (e.g., Schwartz et al., 2008; Mares et al., 2016; Vanella et al., 2022) and comparing these data to changes in sap

flow and moisture in plants. Seismic refraction illuminates water storage potential in the subsurface; however, it is unable to quantify how much moisture is present and how moisture is changing over time. Conducting time-lapse ERI between the north-facing and south-facing slopes might provide insight into how much moisture is being stored to be able to be used by the trees. Although ERI is useful in tracking changes in subsurface moisture, it is less good at locating lithological boundaries. Conversely, seismic refraction excels at finding the soil-bedrock interface and other distinct lithological boundaries, but it is not capable of distinguishing changes in moisture well (Hirsch et al., 2008). Seismic refraction and ERI have been used together often and sap flow and ERI have been used together as well, so I believe the combination of these three methods could be an important step to quantifying how belowground heterogeneity and water storage are influence sap flow rates between slopes at Gordon Gulch.

3.3 Spectrograms and Wavelet Analysis

Spectrograms, which characterize changes in frequency as a function of time, offer a different means to examine time-series datasets (Shragge, 2023). Spectrograms use Fourier transforms to change a single time series into an array representing a timeseries as a function of signal strength (Kang, 2020). They are often used to visualize audio data but can also be used for other timeseries data as well as seismic data (e.g. Lu & Li, 2013). Spectrograms can be complicated and detailed analysis into this method is beyond the scope of this study, however, future analysis into using spectrograms to represent time-series data could be valuable for expanding interpretation of these data, specifically the sap flow data as there has been little investigation into using such analysis tools to interpret sap flow data. Appendix B includes examples of spectrograms of the sap flow data from our plots. Wavelet analysis is an additional

avenue for interpreting non-stationary time series data and similarly characterizes signal frequency related to time. Wavelet analysis has been recently used to analyze sap flow data (e.g. Harmon et al., 2021) and has been applied to other hydrological and geophysical questions (e.g. Henderson et al., 2009); current data for interpreting connections between sap flow and belowground water availability to date is limited.

REFERENCES

- Adams, H. R., Barnard, H. R., & Loomis, A. K. (2014). Topography alters tree growth–climate relationships in a semi-arid forested catchment. *Ecosphere*, 5(11), art148. <https://doi.org/10.1890/ES14-00296.1>
- Aguiar, Mart. R., & Sala, O. E. (1997). Seed Distribution Constrains the Dynamics of the Patagonia Steppe. 78(1), 8.
- Akbari, H., Pomerantz, M., & Taha, H. (2001). Cool surfaces and shade trees to reduce energy use and improve air quality in urban areas. *Solar Energy*, 70(3), 295–310. [https://doi.org/10.1016/S0038-092X\(00\)00089-X](https://doi.org/10.1016/S0038-092X(00)00089-X)
- Anderson, S. P., Kelly, P. J., Hoffman, N., Barnhart, K., Befus, K., & Ouimet, W. (2021). Is This Steady State? Weathering and Critical Zone Architecture in Gordon Gulch, Colorado Front Range. In A. Hunt, M. Egli, & B. Faybishenko (Eds.), *Geophysical Monograph Series* (1st ed., pp. 231–252). Wiley. <https://doi.org/10.1002/9781119563952.ch13>
- Bales, R., & Dietrich, W. (2020). Linking Critical Zone Water Storage and Ecosystems. *Eos*, 101. <https://doi.org/10.1029/2020EO150459>
- Bandler, A. J. (n.d.). Geophysical Constrains on Critical Zone Architecture and Subsurface Hydrology of Opposing Montane Hillslopes. 57.
- Befus, K. M., Sheehan, A. F., Leopold, M., Anderson, S. P., & Anderson, R. S. (2011). Seismic Constraints on Critical Zone Architecture, Boulder Creek Watershed, Front Range, Colorado. *Vadose Zone Journal*, 10(3), 915–927. <https://doi.org/10.2136/vzj2010.0108>
- Brantley, S. L., Goldhaber, M. B., & Ragnarsdottir, K. V. (2007). Crossing Disciplines and Scales to Understand the Critical Zone. *Elements*, 3(5), 307–314. <https://doi.org/10.2113/gselements.3.5.307>
- Buraas, E. M. (2009): Getting water into the ground and to the channel, Gordon Gulch, Colorado. *Thesis, Degree of Bachelor of Arts, Geosciences, Williams College 2009* .
- Burgess, S. S. O., Adams, M. A., Turner, N. C., Beverly, C. R., Ong, C. K., Khan, A. A. H., & Bleby, T. M. (2001). An improved heat pulse method to measure low and reverse rates of sap flow in woody plants. *Tree Physiology*, 21(9), 589–598. <https://doi.org/10.1093/treephys/21.9.589>
- Burns, E. (2022). *Ecohydrologic Dynamics of Rock Moisture in Montane Catchment of the Colorado Front Range*. University of Colorado Boulder.
- Burns, Russell M., and Barbara H. Honkala, tech. coords. 1990. *Silvics of North America: 1. Conifers*. Agriculture Handbook 654. U.S. Department of Agriculture, Forest Service, Washington, DC. vol. 1, 675 p.
- Christensen, Lindsey, Adams, Hallie R., Tai, Xiaonan, Barnard, Holly R., & Brooks, Paul D. (2021). Increasing plant water stress and decreasing summer streamflow in response to a warmer and wetter climate in seasonally snow-covered forests. *Ecohydrology*, 14(1). <https://doi.org/10.1002/eco.2256>

Dawson, T. E., Hahm, W. J., & Crutchfield-Peters, K. (2020). Digging deeper: What the critical zone perspective adds to the study of plant ecophysiology. *New Phytologist*, 226(3), 666–671. <https://doi.org/10.1111/nph.16410>

Debeljak, M., Kocev, D., Towers, W., Jones, M., Griffiths, B. S., & Hallett, P. D. (2009). Potential of multi-objective models for risk-based mapping of the resilience characteristics of soils: Demonstration at a national level. *Soil Use and Management*, 25(1), 66–77. <https://doi.org/10.1111/j.1475-2743.2009.00196.x>

Diek, S., Temme, A. J. A. M., & Teuling, A. J. (2014). The effect of spatial soil variation on the hydrology of a semi-arid Rocky Mountains catchment. *Geoderma*, 235–236, 113–126. <https://doi.org/10.1016/j.geoderma.2014.06.028>

D’Odorico, P., Caylor, K., Okin, G. S., & Scanlon, T. M. (2007). On soil moisture-vegetation feedbacks and their possible effects on the dynamics of dryland ecosystems: SOIL MOISTURE-vegetation feedbacks. *Journal of Geophysical Research: Biogeosciences*, 112(G4), n/a–n/a. <https://doi.org/10.1029/2006JG000379>

Flinchum, B. A., Holbrook, W. S., & Carr, B. J. (2022). What Do P-Wave Velocities Tell Us About the Critical Zone? *Frontiers in Water*, 3, 772185. <https://doi.org/10.3389/frwa.2021.772185>

Flinchum, B. A., Steven Holbrook, W., Rempe, D., Moon, S., Riebe, C. S., Carr, B. J., Hayes, J. L., St. Clair, J., & Peters, M. P. (2018). Critical Zone Structure Under a Granite Ridge Inferred From Drilling and Three-Dimensional Seismic Refraction Data. *Journal of Geophysical Research: Earth Surface*, 123(6), 1317–1343. <https://doi.org/10.1029/2017JF004280>

Giménez, C., Gallardo, M., & Thompson, R. B. (2013). Plant–Water Relations. In *Reference Module in Earth Systems and Environmental Sciences* (p. B978012409548905257X). Elsevier. <https://doi.org/10.1016/B978-0-12-409548-9.05257-X>

Goulden, M. L., & Bales, R. C. (2019). California forest die-off linked to multi-year deep soil drying in 2012–2015 drought. *Nature Geoscience*, 12(8), 632–637. <https://doi.org/10.1038/s41561-019-0388-5>

Graham, R., Rossi, A., & Hubbert, R. (2010). Rock to regolith conversion: Producing hospitable substrates for terrestrial ecosystems. *GSA Today*, 4–9. <https://doi.org/10.1130/GSAT57A.1>

Hahm, W. J., Dralle, D. N., Sanders, M., Bryk, A. B., Fauria, K. E., Huang, M. H., Hudson-Rasmussen, B., Nelson, M. D., Pedrazas, M. A., Schmidt, L., Whiting, J., Dietrich, W. E., & Rempe, D. M. (2022). Bedrock Vadose Zone Storage Dynamics Under Extreme Drought: Consequences for Plant Water Availability, Recharge, and Runoff. *Water Resources Research*, 58(4). <https://doi.org/10.1029/2021WR031781>

Hahm, W. J., Rempe, D. M., Dralle, D. N., Dawson, T. E., Lovill, S. M., Bryk, A. B., Bish, D. L., Schieber, J., & Dietrich, W. E. (2019). Lithologically Controlled Subsurface Critical Zone Thickness and Water Storage Capacity Determine Regional Plant Community Composition. *Water Resources Research*, 55(4), 3028–3055. <https://doi.org/10.1029/2018WR023760>

- Harmon, R. E., Barnard, H. R., Day-Lewis, F. D., Mao, D., & Singha, K. (2021). Exploring Environmental Factors That Drive Diel Variations in Tree Water Storage Using Wavelet Analysis. *Frontiers in Water*, 3, 682285. <https://doi.org/10.3389/frwa.2021.682285>
- Henderson, R. D., Day-Lewis, F. D., & Harvey, C. F. (2009). Investigation of aquifer-estuary interaction using wavelet analysis of fiber-optic temperature data. *Geophysical Research Letters*, 36(6), L06403. <https://doi.org/10.1029/2008GL036926>
- Hinckley, E.-L. S., Ebel, B. A., Barnes, R. T., Anderson, R. S., Williams, M. W., & Anderson, S. P. (2014). Aspect control of water movement on hillslopes near the rain-snow transition of the Colorado Front Range: Snowmelt and Hydrological Flow Paths on Opposing Hillslope Aspects. *Hydrological Processes*, 28(1), 74–85. <https://doi.org/10.1002/hyp.9549>
- Hirsch, M., Bentley, L. R., & Dietrich, P. (2008). A Comparison of Electrical Resistivity, Ground Penetrating Radar and Seismic Refraction Results at a River Terrace Site. *Journal of Environmental & Engineering Geophysics*, 13(4), 325–333. <https://doi.org/10.2113/JEEG13.4.325>
- Holbrook, W. S., Riebe, C. S., Elwaseif, M., L. Hayes, J., Basler-Reeder, K., L. Harry, D., Malazian, A., Dosseto, A., C. Hartsough, P., & W. Hopmans, J. (2014). Geophysical constraints on deep weathering and water storage potential in the Southern Sierra Critical Zone Observatory: Geophysical Constrains on Weathering in the Southern Sierra CZO. *Earth Surface Processes and Landforms*, 39(3), 366–380. <https://doi.org/10.1002/esp.3502>
- IPCC, 2021: *Climate Change 2021: The Physical Science Basis. Contribution of Working Group I to the Sixth Assessment Report of the Intergovernmental Panel on Climate Change*[Masson-Delmotte, V., P. Zhai, A. Pirani, S.L. Connors, C. Péan, S. Berger, N. Caud, Y. Chen, L. Goldfarb, M.I. Gomis, M. Huang, K. Leitzell, E. Lonnoy, J.B.R. Matthews, T.K. Maycock, T. Waterfield, O. Yelekçi, R. Yu, and B. Zhou (eds.)]. Cambridge University Press, Cambridge, United Kingdom and New York, NY, USA, In press, doi:10.1017/9781009157896.
- Johnstone, J. F., McIntire, E. J. B., Pedersen, E. J., King, G., & Pisaric, M. J. F. (2010). A sensitive slope: Estimating landscape patterns of forest resilience in a changing climate. *Ecosphere*, 1(6), art14. <https://doi.org/10.1890/ES10-00102.1>
- Kang, C., (2020). Jupyter Notebooks – a publishing format for reproducible computational workflows. *Time Series as Inputs to a Model*
- Klos, P. Z., Goulden, M. L., Riebe, C. S., Tague, C. L., O’Geen, A. T., Flinchum, B. A., Safeeq, M., Conklin, M. H., Hart, S. C., Berhe, A. A., Hartsough, P. C., Holbrook, W. S., & Bales, R. C. (2018). Subsurface plant-accessible water in mountain ecosystems with a Mediterranean climate. *WIREs Water*, 5(3). <https://doi.org/10.1002/wat2.1277>
- Leopold, M., Volkel, J., Huber, J., & Dethier, D. (2013). Subsurface architecture of the Boulder Creek Critical Zone Observatory from electrical resistivity tomography. *Earth Surface Processes and Landforms*, 38(12). <https://doi.org/10.1002/esp.3420>
- Long, J. N., & Dean, T. J. (1986). Sapwood area of *Pinus contorta* stands as a function of mean size and density. *Oecologia*, 68(3), 410–412. <https://doi.org/10.1007/BF01036747>

Lovering, T. S., & Tweto, O. (1953). *Geology and Ore Deposits of the Boulder County Tungsten District Colorado* (Professional Paper) [Professional Paper]. Geological Survey.

Lu, W., & Li, F. (2013). Seismic spectral decomposition using deconvolutive short-time Fourier transform spectrogram. *GEOPHYSICS*, 78(2), V43–V51. <https://doi.org/10.1190/geo2012-0125.1>

Mares, R., Barnard, H. R., Mao, D., Revil, A., & Singha, K. (2016). Examining diel patterns of soil and xylem moisture using electrical resistivity imaging. *Journal of Hydrology*, 536, 327–338. <https://doi.org/10.1016/j.jhydrol.2016.03.003>

McCormick, E. L., Dralle, D. N., Hahm, W. J., Tune, A. K., Schmidt, L. M., Chadwick, K. D., & Rempe, D. M. (2021). Widespread woody plant use of water stored in bedrock. *Nature*, 597(7875), 225–229. <https://doi.org/10.1038/s41586-021-03761-3>

Mitra, B., Papuga, S. A., Alexander, M. R., Swetnam, T. L., & Abramson, N. (2020). Allometric relationships between primary size measures and sapwood area for six common tree species in snow-dependent ecosystems in the Southwest United States. *Journal of Forestry Research*, 31(6), 2171–2180. <https://doi.org/10.1007/s11676-019-01048-y>

Noble, D. L. (1979). Roots of lodgepole pine seedlings reach depth of only 3 to 4 inches their first season. *Rocky Mountain Research Station Publications*.

Parsekian, A. D., Singha, K., Minsley, B. J., Holbrook, W. S., & Slater, L. (2015). Multiscale geophysical imaging of the critical zone: Geophysical Imaging of the Critical Zone. *Reviews of Geophysics*, 53(1), 1–26. <https://doi.org/10.1002/2014RG000465>

Poorter, L., Bongers, F., Aide, T. M., Almeyda Zambrano, A. M., Balvanera, P., Becknell, J. M., Boukili, V., Brancalion, P. H. S., Broadbent, E. N., Chazdon, R. L., Craven, D., De Almeida-Cortez, J. S., Cabral, G. A. L., De Jong, B. H. J., Denslow, J. S., Dent, D. H., DeWalt, S. J., Dupuy, J. M., Durán, S. M., ... Rozendaal, D. M. A. (2016). Biomass resilience of Neotropical secondary forests. *Nature*, 530(7589), 211–214. <https://doi.org/10.1038/nature16512>

Pramova, E., Locatelli, B., Djoudi, H., & Somorin, O. A. (2012). Forests and trees for social adaptation to climate variability and change. *WIREs Climate Change*, 3(6), 581–596. <https://doi.org/10.1002/wcc.195>

Punyasena, S. W., Eshel, G., & McElwain, J. C. (2007). The influence of climate on the spatial patterning of Neotropical plant families. *Journal of Biogeography*, 0(0), 070901070439001-???. <https://doi.org/10.1111/j.1365-2699.2007.01773.x>

Rempe, D. M., & Dietrich, W. E. (2014). A bottom-up control on fresh-bedrock topography under landscapes. *Proceedings of the National Academy of Sciences*, 111(18), 6576–6581. <https://doi.org/10.1073/pnas.1404763111>

Richardson, D. M., Rundel, P. W., Jackson, S. T., Teskey, R. O., Aronson, J., Bytnerowicz, A., Wingfield, M. J., & Procheş, Ş. (2007). Human Impacts in Pine Forests: Past, Present, and Future. *Annual Review of Ecology, Evolution, and Systematics*, 38(1), 275–297. <https://doi.org/10.1146/annurev.ecolsys.38.091206.095650>

Riebe, C. S., Hahm, W. J., & Brantley, S. L. (2017). Controls on deep critical zone architecture: A historical review and four testable hypotheses: Four Testable Hypotheses about the Deep

Critical Zone. *Earth Surface Processes and Landforms*, 42(1), 128–156. <https://doi.org/10.1002/esp.4052>

Rücker, C., Günther, T., & Wagner, F. M. (2017). pyGIMLi: An open-source library for modelling and inversion in geophysics. *Computers & Geosciences*, 109, 106–123. <https://doi.org/10.1016/j.cageo.2017.07.011>

Salberg, L., Anderson, S., & Ge, S. (2022). *The Role of Groundwater Flow in a Montane, Semi-Arid, Headwater Catchment* [Preprint]. Preprints. <https://doi.org/10.22541/au.167195315.58049864/v1>

Schwartz, B. F., Schreiber, M. E., & Yan, T. (2008). Quantifying field-scale soil moisture using electrical resistivity imaging. *Journal of Hydrology*, 362(3–4), 234–246. <https://doi.org/10.1016/j.jhydrol.2008.08.027>

Shragge, J., Digital Signal Processing (2023), GitHub repository, https://github.com/jshragge/CSM_GP_DIGSIG/blob/master/12_Windows_and_Spectrograms.ipynb

St. Clair, J., Moon, S., Holbrook, W. S., Perron, J. T., Riebe, C. S., Martel, S. J., Carr, B., Harman, C., Singha, K., & Richter, D. deB. (2015). Geophysical imaging reveals topographic stress control of bedrock weathering. *Science*, 350(6260), 534–538. <https://doi.org/10.1126/science.aab2210>

Sun, X., Li, J., Cameron, D., & Moore, G. (2021). On the Use of Sap Flow Measurements to Assess the Water Requirements of Three Australian Native Tree Species. *Agronomy*, 12(1), 52. <https://doi.org/10.3390/agronomy12010052>

Vanella, D., Ramírez-Cuesta, J. M., Longo-Minnolo, G., Longo, D., D’Emilio, A., & Consoli, S. (2023). Identifying soil-plant interactions in a mixed-age orange orchard using electrical resistivity imaging. *Plant and Soil*, 483(1–2), 181–197. <https://doi.org/10.1007/s11104-022-05733-6>

APPENDIX A

STACKING, PICKING AND INVERTING SEISMIC DATA

This document (edited from a draft started by Joel Singley (jsingley@rwu.edu)) summarizes the workflow for stacking shots, picking first arrivals, and then inverting seismic data. Before you begin, you will need to install Seismic Unix, python, conda, pyGIMLi, and Brady Flinchum's picking and segy conversion software on your computer. Brady has provided a [playlist](#) of screen capture videos on how to do all of these setup tasks on a Mac. Watch and follow all those directions before you start on the next steps. Note that there are some errors in the videos, but Brady catches them and solves them as he works – so watch everything carefully! Also, you can do some of the python-related installations and setup using Anaconda Navigator if you prefer, rather than via the terminal as Brady does it. Brady's codes are written in Python, and he uses the Spyder editor. To open it, you can go to Anaconda Navigator --> Launch Spyder.

A.1 Stack shots

A.1.1 Converting Data

To start, we will convert the raw data files from the Geometric .dat to the more archaic but commonly used .sgy (or SEG-Y) format. You'll need a folder with all your .dat files for a particular line. Let's call this your `data_folder`. Place a copy of Brady's `convert2seggy.bsh` into your `data_folder`. Then create `seggyFiles` (capitalization matters!) as a subdirectory within your `data_folder`. This program uses Seismic Unix, so that needs to be installed on your computer as noted above.

Open terminal and navigate to your `data_folder`. To do so type "cd" (no quotes) followed by the complete path. Instead of typing out the path, you can click and drag the folder from a finder

window into your terminal and the path will automatically be populated. Once you are in the correct directory, run the command: `bash convert2segy.bsh` and your data files will be converted to segy format and output into `data_folder/segyFiles`. This can take a bit of time depending on how much data you have.

A.1.2 Creating a Stacking Guide

Now, we need to identify which datafiles correspond to each shot location and need to be stacked together. To do this, we'll create a `stack_input.csv` that identifies shot locations and file names. You can either do this in Excel or via a text editor.

The first column will be the shot location (m), the second column will always be populated with "3" (no quotes), and then the subsequent columns will list the file names (without the extension .sgy) that need to be stacked. For example, the first two lines of the file might look like:

```
0,3,795,796,797,798,799,800,801,802,803,-999
```

```
1,3,805,806,807,808,809,810,811,812,813,814
```

The first row indicates that the data for shots at the beginning of the line (distance = 0 m) are in the files named 795-803 while the data for shots at 1 m are in the files named 805-814. Again, the "3" in the second column is just a flag for geophone placement, but it must be included.

Notice that there is no header row. Also, the number of actual file names does not need to be the same in each row, but "empty" cells need to be filled with "-999" as a null value, as shown in the first row above and in Table A.1.

Table A.1 Additional example of how to set up a stack input guide. From left to right there is the shot location (-20, -10, 0, etc.), the “3”, and the file numbers of the shots we want to stack at the given shot location (3000, 3001 etc.) and “-999” for a null value.

Line Stackinput Example						
-20	3	3000	3001	3002	3003	-999
-10	3	3005	3006	3007	3008	3009
0	3	3010	3011	3012	3013	3014
11.5	3	3015	3016	3017	3018	3019
23.5	3	3020	3021	3022	3023	3024
35.5	3	3025	3026	3027	3028	3029
47	3	3030	3031	3032	3033	3034
57	3	3035	3036	3037	3038	3039
67	3	3040	3041	3042	3043	3044

Note: When saving the .csv file with the stack inputs, you may need to play around with the file type as some files don't work when calling the .csv. For Mac, save the file as a Mac csv.

You may be able to create this file quickly based on your notes from the field if they're nicely detailed (I.e., you wrote down which .dat files correspond with each shot location). If that isn't the case, you can use terminal to check the shot location in the segy files by running “cd segyFiles” then “segypread tape=795.sgy | surange”.

Replace “795” with file name to match the first file in data_folder/segypFiles. You can repeat that second command for subsequent files to identify all the files with the same “sx” (shot spacing) value. Then put those file names into columns 3+ of your stack_input.csv file in the row corresponding to the given sx value. For the above example, files 795-803 all have sx = 0 when viewed via terminal in this way. The output from segypread tape is shown in Figure A.1.

```
3200 bytes transferred in 0.001647 secs (1942932 bytes/sec)
getpar() call after checkpars(): nextended
48 traces:
fldr      003
tracf     1 48 (1 - 48)
trid       1
nvs        1
gx         0 23 (0 - 23)
delrt     -10
ns        10000
dt         20
lgs        24
afilf     20000
grnors    2 49 (2 - 49)
grnofr    2 49 (2 - 49)
grnlof    0 1 (0 - 1)
dl         0.000000

Receiver coordinate limits:
      North(0,0) South(0,0) East(23,0) West(0,0)

Midpoint coordinate limits:
      North(0,0) South(0,0) East(11.5,0) West(0,0)
```

Figure A.1 Example of segyread output in the terminal window. Note that in this case, there is no `sx` term because `sx = 0`, but `sx` will be defined for any file where the source location is not equal to zero.

A.1.3 Automated stacking with Python Script

Launch Spyder either from the terminal or Anaconda Navigator and open Brady's `stackData.py`. Note: To launch in terminal open a terminal window and type 'conda activate pg' then type 'spyder' and the program will open. You'll need to manually edit two paths, to point to the stacking guide (`stack_input.csv`) that you created and the folder with the segy files. First, enter the path to your `.csv` in the space on L84 of the script (Figure A.2). The example path will differ, but make sure you include the file extension and identify the delimiter. Next, enter the full path to your `data_folder/segFiles` directory into the "path2data" line (L89 in screenshot). Note that this path should end with a slash.

```

84 files = np.loadtxt('/Users/joelsingley/Desktop/Dropbox/PickingSoftware/PmLine6/stack_input_roll1.csv',delimiter=',')
85
86 #shotLocs = np.unique(files[:,0])
87 shotLocs = files[:,0]
88 polarities = files[:,1]
89 path2Data = '/Users/joelsingley/Desktop/Dropbox/PickingSoftware/PmLine6/roll1/seggyFiles/'

```

Figure A.2 Example of the path to your .csv file with the stack input data and the path to the segy files using python.

If any of your geophones were placed at non-integer distances in m (i.e., 0.5 m spacing on the whole line), you'll need to hard code these locations into the .py file since segy file headers don't store decimals. To do this, uncomment L125 (Figure A.3) and adjust the x = sequence. The example that is uncommented is for 48 geophones with 0.5 m spacing starting at a location of 0 m.

```

116     for j in range(0,len(files2Read)):
117
118         if polarities[i] == 1 or polarities[i]==2:
119             file = path2Data + str(int(files2Read[j])) + '.sgy'
120         else:
121             file = path2Data + str(int(files2Read[j])) + '.sgy'
122
123         [x, t, dataTemp, gx, shotLoc] = getData('seggy',file)
124         #*****
125         x = np.linspace(0,23.5,48) #*****HARD CODED FOR 48 geophones at 0.5 m spacing
126         #x = np.linspace(24,47.5,48) #GEOPHONE LOCATIONS FOR THE SECOND ROLL WITH GX_0 = 24
127         #*****
128         data[:,:,j] = dataTemp
129         dataNorm[:,:,j] = normalizeTraces(dataTemp)
130
131
132         ax1 = fig2.add_subplot(4,4,j+1)
133         ax1.pcolorfast(x,t,dataNorm[:,:,j],cmap='gray',vmin=-0.5,vmax=0.5)
134         ax1.invert_yaxis()
135         ax1.set_title('File # ' + str(int(files2Read[j])))
136         ax1.set_xlabel('Distance (m)')
137         ax1.set_ylabel('Time (s)')
138

```

Figure A.3 Example of how to hard code geophone locations if they are placed at non-integer distances.

Lastly, you need to hard code the max dimensions of subplots showing data from individual shots that will be stacked together. To do this, identify the maximum number (n_max) of data files you have for a particular shot location using your stack_input.csv file. Then search for the portion of the code that appears on L132 above "...add_subplot(4,4,j+1)" - note that it appears there and again at ~L162 (L114?). Your subplot dimensions (rows x columns, 4 x 4 in the screenshot) must be greater than or equal to n_max.

Now go ahead and run the whole script by pressing F5 or the green “run file” button. The code will automatically populate data_folder/segYFiles with both plots and stacked shots in segy format. Use the plots of the individual and stacked shots (named like X.Ym.png and X.Ym_allshots.png with X.Y indicating shot location) to ensure that all included shots have good data. For instance, in this set the data from file # 990 should be excluded.

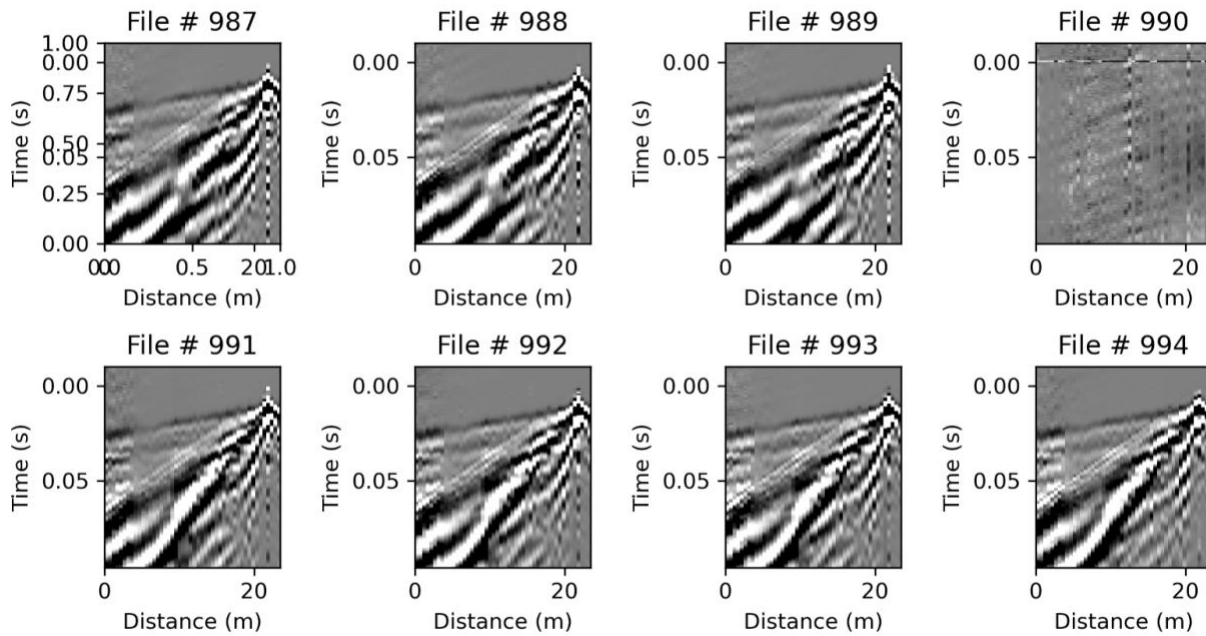


Figure A.4 Example plots of the individual shots to be stacked at a single shot location using the stackData.py script.

If you find shots that should be excluded, go back to the stack_input.csv file, replace those file names with the null value (-999) and then re-run the stacking script.

A.2 Picking First Arrivals

Brady's picking code (`stackData.py`) is setup to allow you to graphically pick first arrivals from the stacked shots. As you click on the images the code will automatically update a file containing the shot location, geophone location, and first arrival time. Note that the "pick file" .txt file (defined ~ L 691) you'll use to store the picks must exist and be populated with at least two lines before you start running the python picking script. The easiest way to accomplish this is to just copy a prior file to your desired path and delete all but the first two lines. So long as the distances listed correspond with distances from shots that appear in your dataset, those old lines will automatically be overwritten as you pick. This pick file has three columns, which is what you'll generate with the picker and what gets passed to `pyGIMLi`. The first column is the shot location, the second the geophone location, and the third is the travel time picked in seconds. There's no need to save anything—when you click, it saves.

There are only a couple of other lines you need to edit in the picker code. At line 685, you can turn on a bandpass filter (change the Boolean). `Lf`, `hf`, and `nq` all are affiliated with the bandpass filter. The other thing is to update paths if needed (for instance, the location that `dirName` at line 705 points to the location of your `segy` files) `pyGIMLi` produces a model of your travel times. `convSPpickfile` is the model picked file that you can compare to your picks. If you haven't run `pyGIMLi` yet, just set this to double quotes with nothing in between. This code will read EVERY `segy` file in that directory, even if it is garbage. The code doesn't modify the `segy` files, however. Note that `segy` files are stupid and don't record decimals, so if you have geophone spacings not at integer locations, you must manually fix them by setting the sequence of values for the geophone locations, called "x" (Figure A.5).

```
726
727 # MANUALLY adjust geophone spacing if not in whole meters
728 #x = np.linspace(0,23.5,48) #*****HARD CODED FOR 48 geophones at 0.5 m spacing
729 x = np.linspace(24,47.5,48) #GEOPHONE LOCATIONS FOR THE SECOND ROLL WITH GX_0 = 24
730 print(x)
```

Figure A.5 Example script for manually fixing geophone spacing for those that are not at integer locations.

Then, set the shot location you want to pick at line 711 and you're good to go. That's all you need to change! You can hit run. Two figure windows should open with your entire shot gather on the left and a wiggle trace (Figure A.6). If your figures open in the Plots pane, you'll need them to pop out. Go to Preferences (the wrench tool) à iPython console à Graphics à Graphics Backend and set it to Automatic. On Figure 1, the amplitude slider changes the gain, and the main time changes the vertical exaggeration. On Figure 2, the amplitude slider also gains/scales, the initial time slider slides your trace up and down.

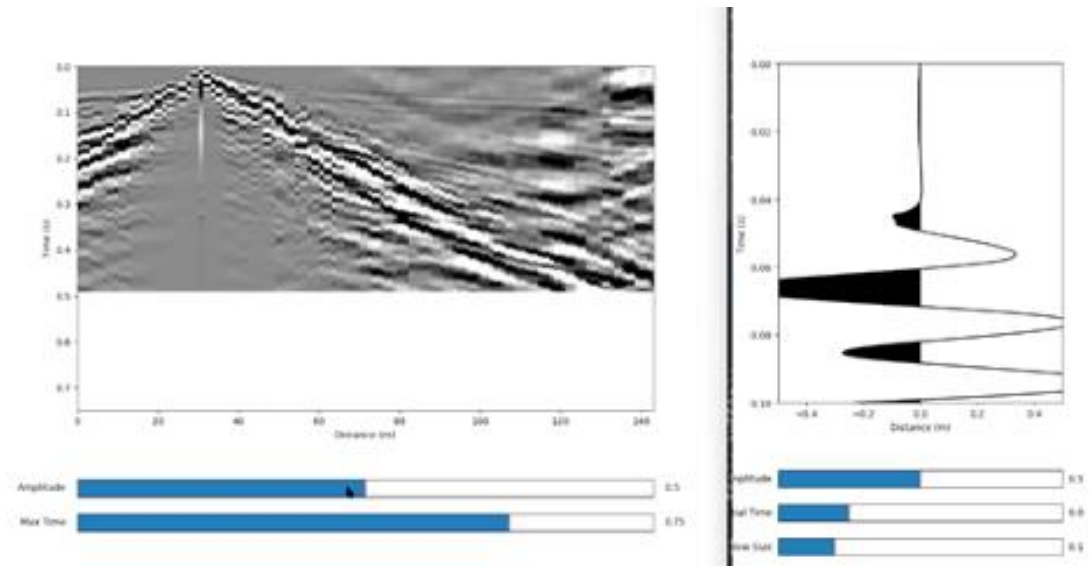


Figure A.6 Example of the window where you pick the first arrival times of the stacked shots at each location.

Our goal is to pick the first arriving energy. You can't pick on Figure 1, but if you click in Figure 1, it'll open the associated wiggle trace in Figure 2 from which you can pick. You can scroll back and forth across the wiggles with the left and right arrow.

On Figure 2 in the pop-up window, left click the first arrival. You'll get a blue line at the location of your pick. A right click anywhere in the window will delete your pick if you need. After you select your first arrival, use the right arrow to move to the next wiggle trace. It's a little bit of an art to pick the first arriving energy! The important detail is not to swap phases. A good fit is probably within 2-3 ms, so whether you pick at the top or bottom doesn't matter that much as long as you are consistent. Just click first arrivals along your line for as far as you're confident in your data and not beyond. The picks will show up on Figure 1 as blue lines, which can be helpful for tracking where you are at. Pick as far out as you can for each stack of shots, but you do not need to pick the arrival at every geophone! Remember that it is better to stop picking if you aren't sure where the actual first arrivals appear than to pick incorrectly. Once you pick all your data (from each geophone for that shot location), you'll rerun the picker code by updating to the next shot location and continue picking. It'll continue to write the data to the text file.

A.3 Inverting with pyGIMLi

Lastly, we will invert the data to generate 2D seismic velocity models of the subsurface. First, you'll need to extract elevations and distances (projected into map space and along the line). To do so, use the [extractElevationProfile_rev2.py](#) script from Brady. You'll need to have [gdal](#) installed in your pg conda environment. If you don't have all of the dependencies installed, you'll hit a snag around L38.

Note: gdal often does not want to install on mac. If you have a base environment in spyder chances are gdal is already installed there and you can run the extract elevation script in this environment, then use your pg environment to call the saved file. Within this script, go to L139 and put the path to the geotiff file containing the digital elevation model for the study area. Make sure this file is in UTM (x,y) projection – if you need to re-project the DEM, you can do so in QGIS by going to Raster > Projections > Warp (reproject). Select the correct UTM projection (including the correct zone number) and then you can save re-projected DEM to a new file.

Now, go to L139 in the `extractElevationProfile_rev2.py` script and set the path the geotiff with the correct projection. Then enter the start of line (SoL) and end of line (EoL) coordinates, again in UTM projection, into L140 and L141. Enter the distance along the line for the first geophone on L145, the distance to the last geophone on L146, and the geophone spacing on L147. Then adjust the output file name as needed and run the script. For this example, we'll call this output *topography.txt*. Visually inspect the location of the line within the broader geotiff in the autogenerated plot as well as the topography of the line.

The *topography.txt* file will have three columns. The first is the slope adjusted distance, second is the elevation (units of the map), and column three is the location of the geophones as they were in the field. Finally, for the inversion open the *StreamLineInversion_Pwave.py* script and edit L187-240. In particular, the call for `pickFile` (L187) is for the output from *picker.py* described above. If you have multiple pick files from multiple rolls, you'll need to concatenate them into one txt file (copying and pasting in a text editor is fine). Make sure you delete the extra empty row at the bottom of the txt file, which can cause errors when using `np.loadtxt()`. The *topography.txt* file path is entered on L200. Use the same SoL and EoL inputs on L205-206 as you did in the elevation extraction script - this ensures that the inversion produces a spatially

located VTK file. Then L216-217 control the weights of the data and are in units of ms. Smaller values will force a closer matching between the inverse model and the data. L230-249 are for the mesh parameters and limits on the number of iterations. Run the inversion! Check the outputs, especially the missfit by shot location and p-wave model fits plots to make sure there isn't a lot of structure to the errors. In the console, check the Chi2 and RMS values for the inversion. If they seem high, you can go back and reduce the maxError and minError tolerances (L216-217) and re-run the inversion.

APPENDIX B
ADDITIONAL FIGURES

Line 1

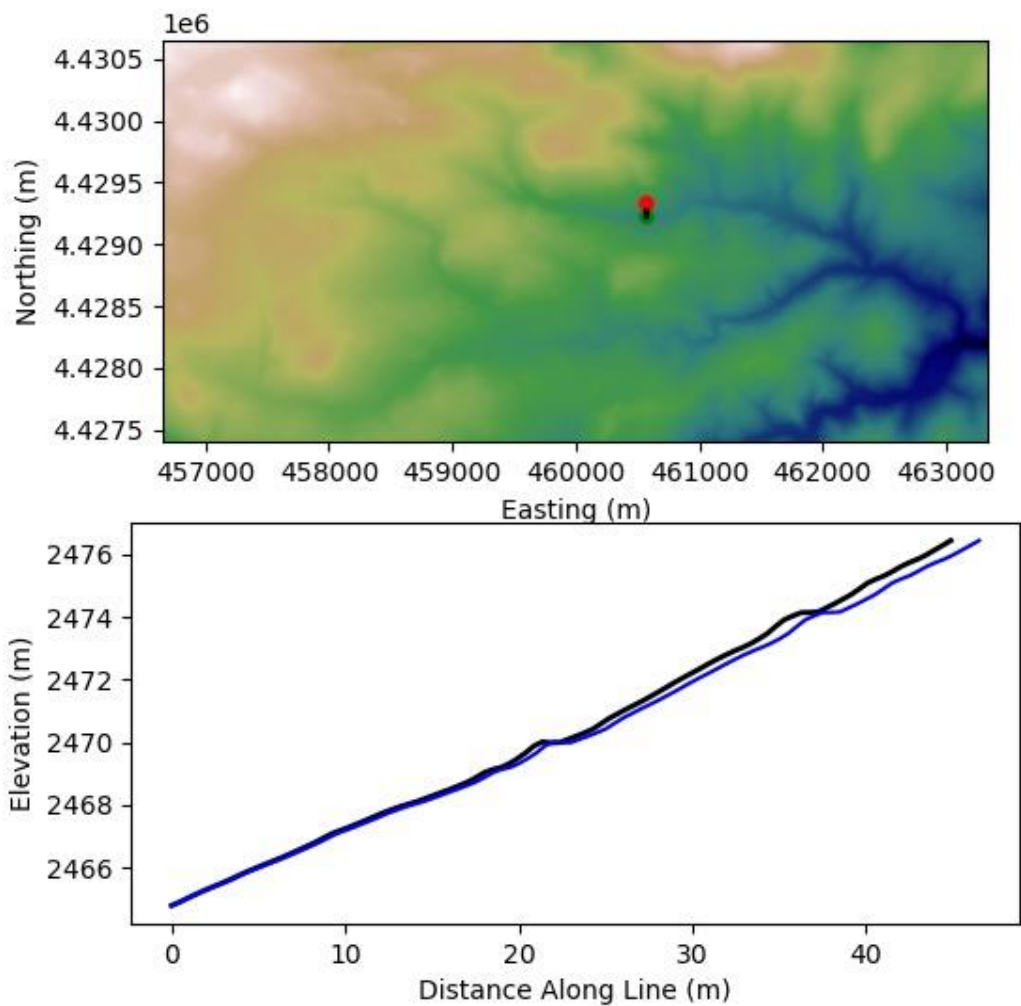


Figure B.1 Elevation profile and distance for seismic Line 1 on the south-facing slope generated by the *extractElevationProfile_rev2.py* script in Anaconda.

Line 1

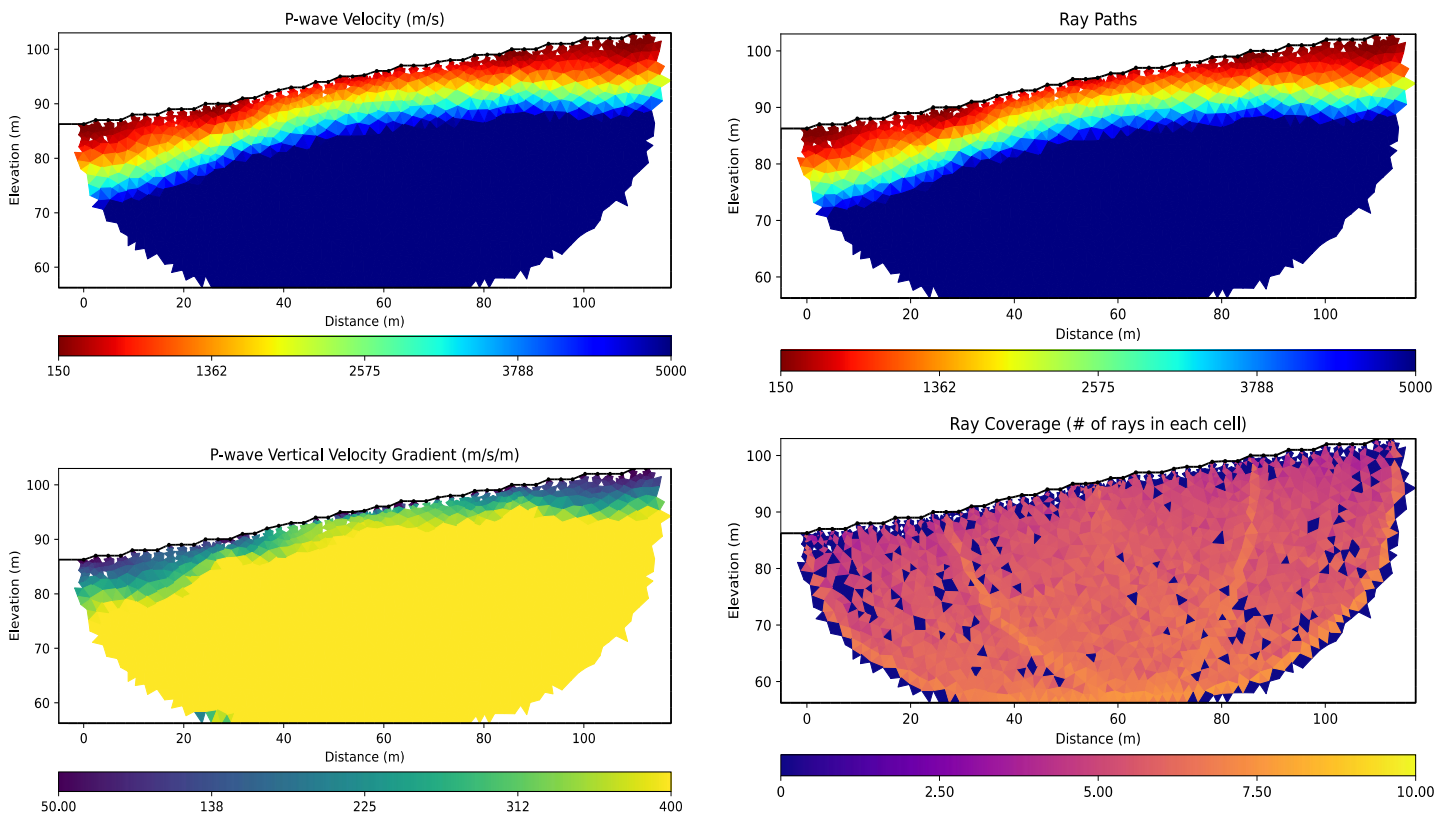


Figure B.2 P-wave velocity profile, p-wave vertical velocity gradient, ray paths, and ray coverage for seismic Line 1 generated by the pyGIMLi inversion using the script *StreamLineInversion_Pwave.py*.

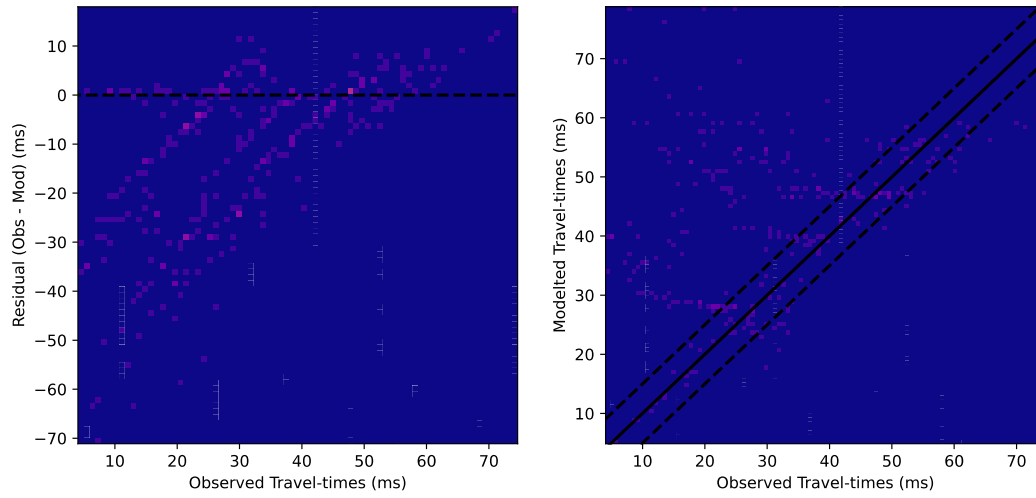


Figure B.3 The residual (observed – modeled) as a function of the observed travel times, and modeled vs observed travel times for seismic Line 1.

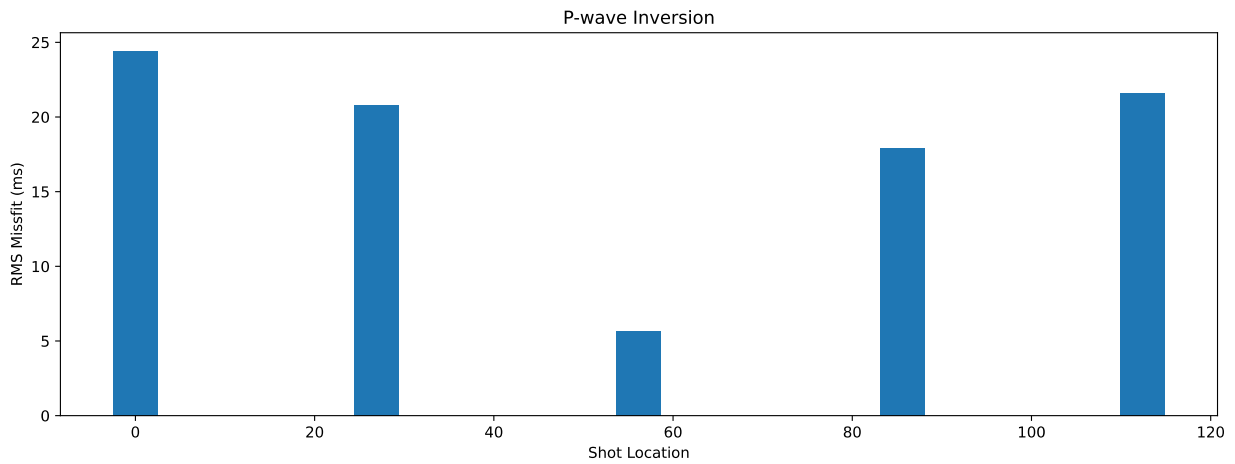


Figure B.4 The root mean square (RMS) misfit for each shot location for the p-wave inversions for Line 1.

Line 2

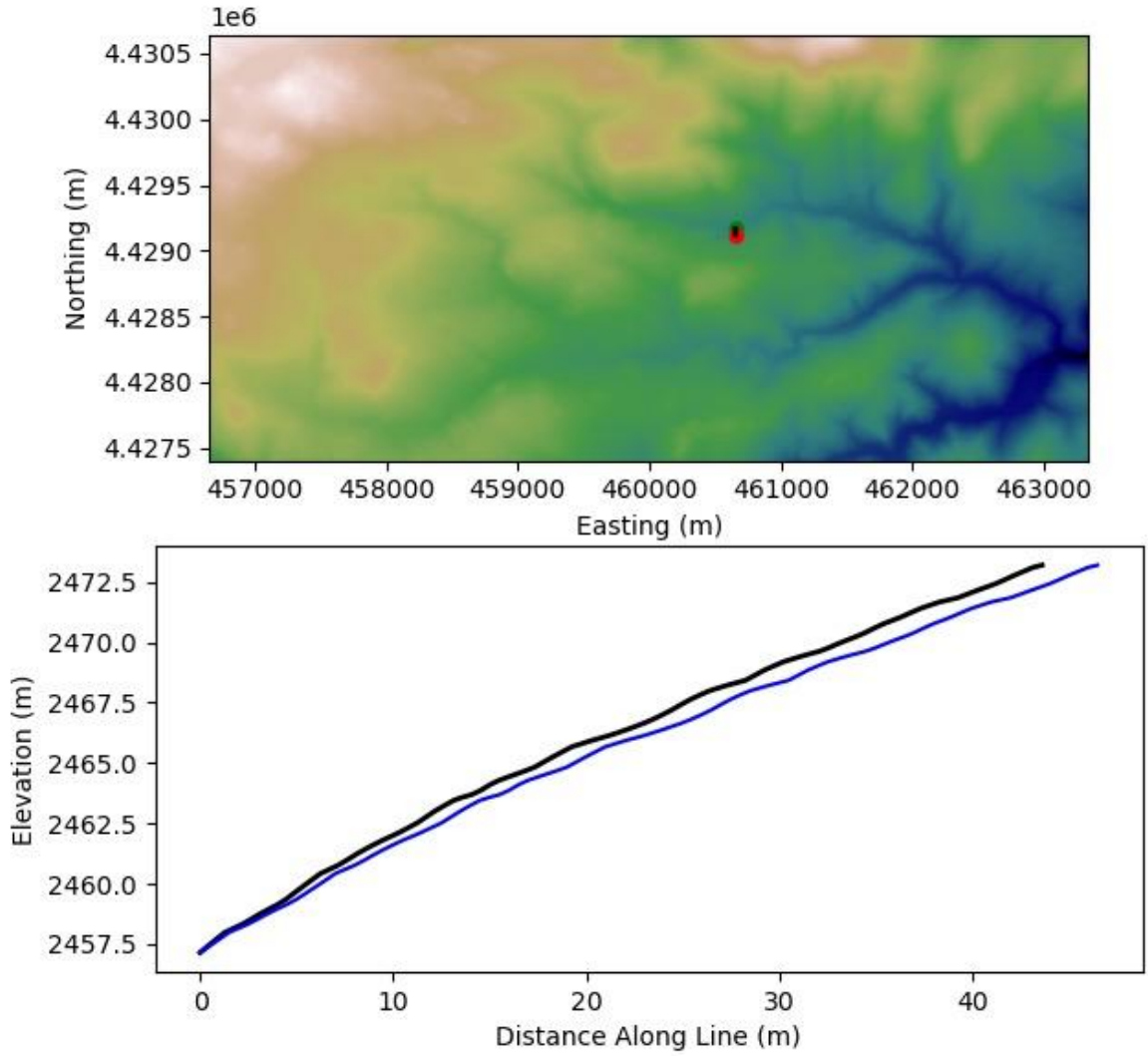


Figure B.5 Elevation profile and distance for seismic Line 2 on the south-facing slope generated by the *extractElevationProfile_rev2.py* script in Anaconda.

Line 2

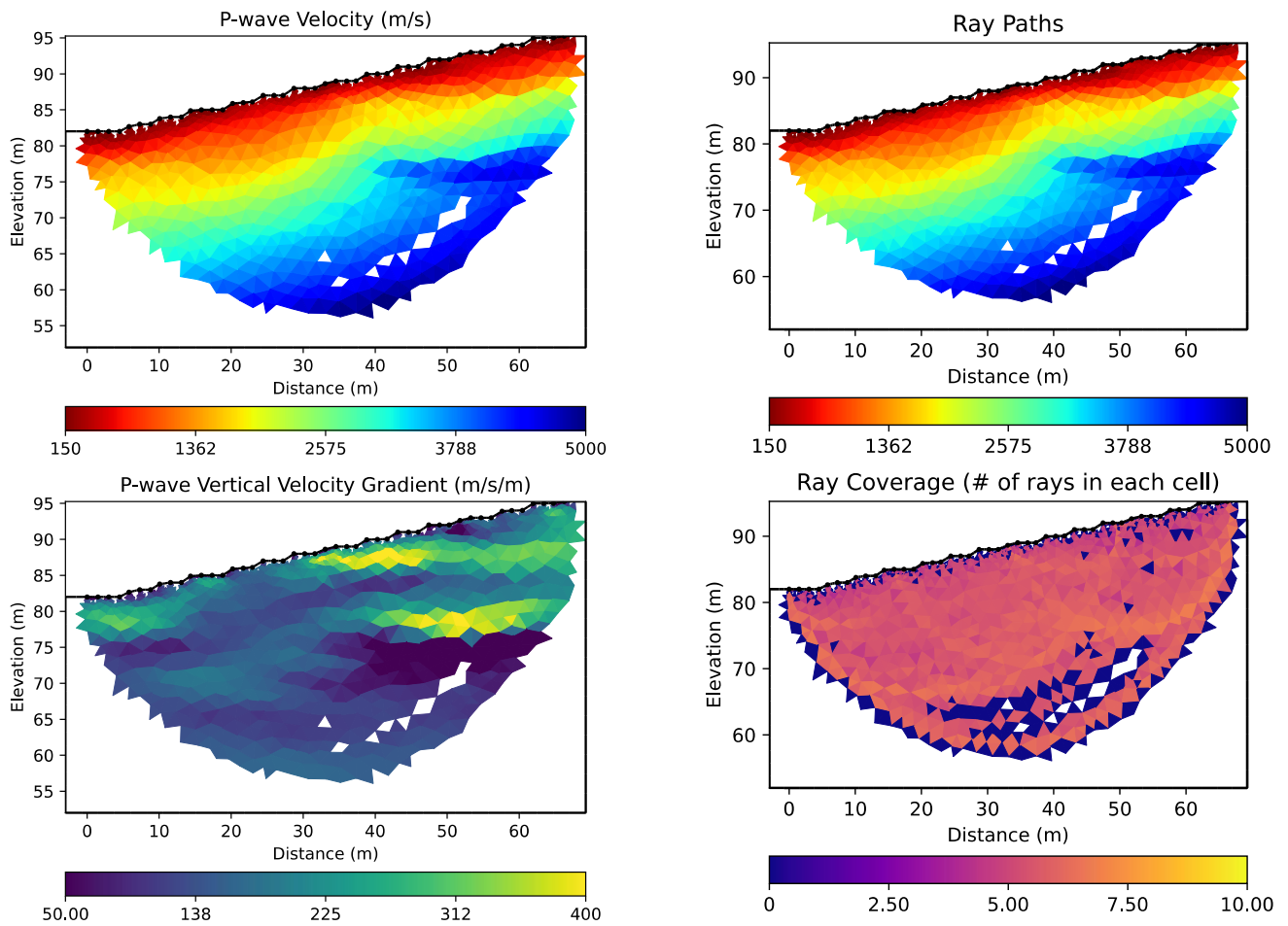


Figure B.6 P-wave velocity profile, p-wave vertical velocity gradient, ray paths, and ray coverage for seismic Line 2 generated by the pyGIMLi inversion using the script *StreamLineInversion_Pwave.py*.

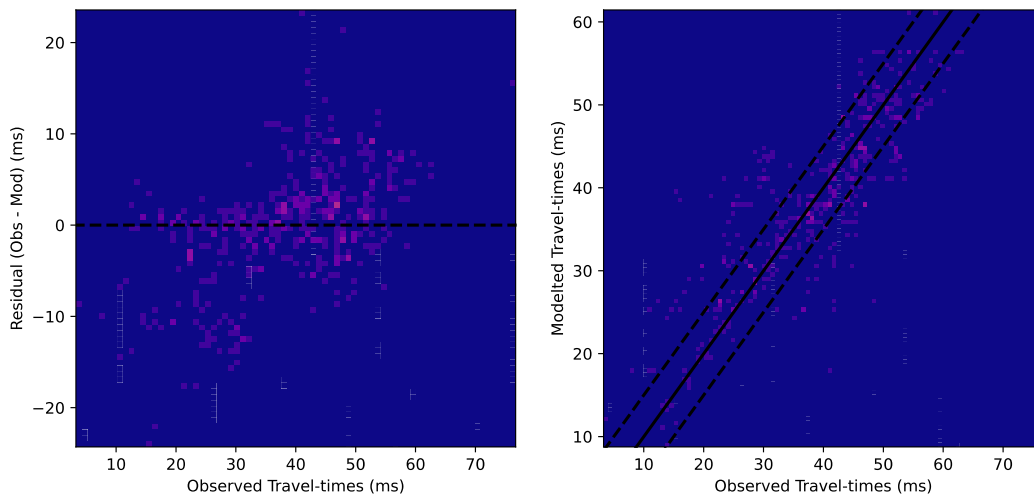


Figure B.7 The residual (observed – modeled) as a function of the observed travel times, and modeled vs observed travel times for seismic Line 2.

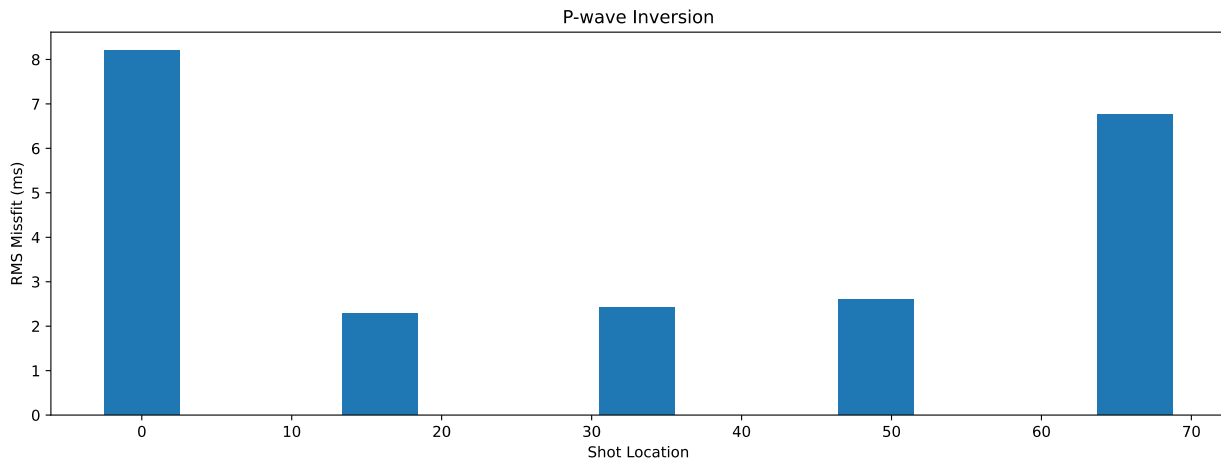


Figure B.8 The root mean square (RMS) misfit for each shot location for the p-wave inversions for Line 2.

Line 3

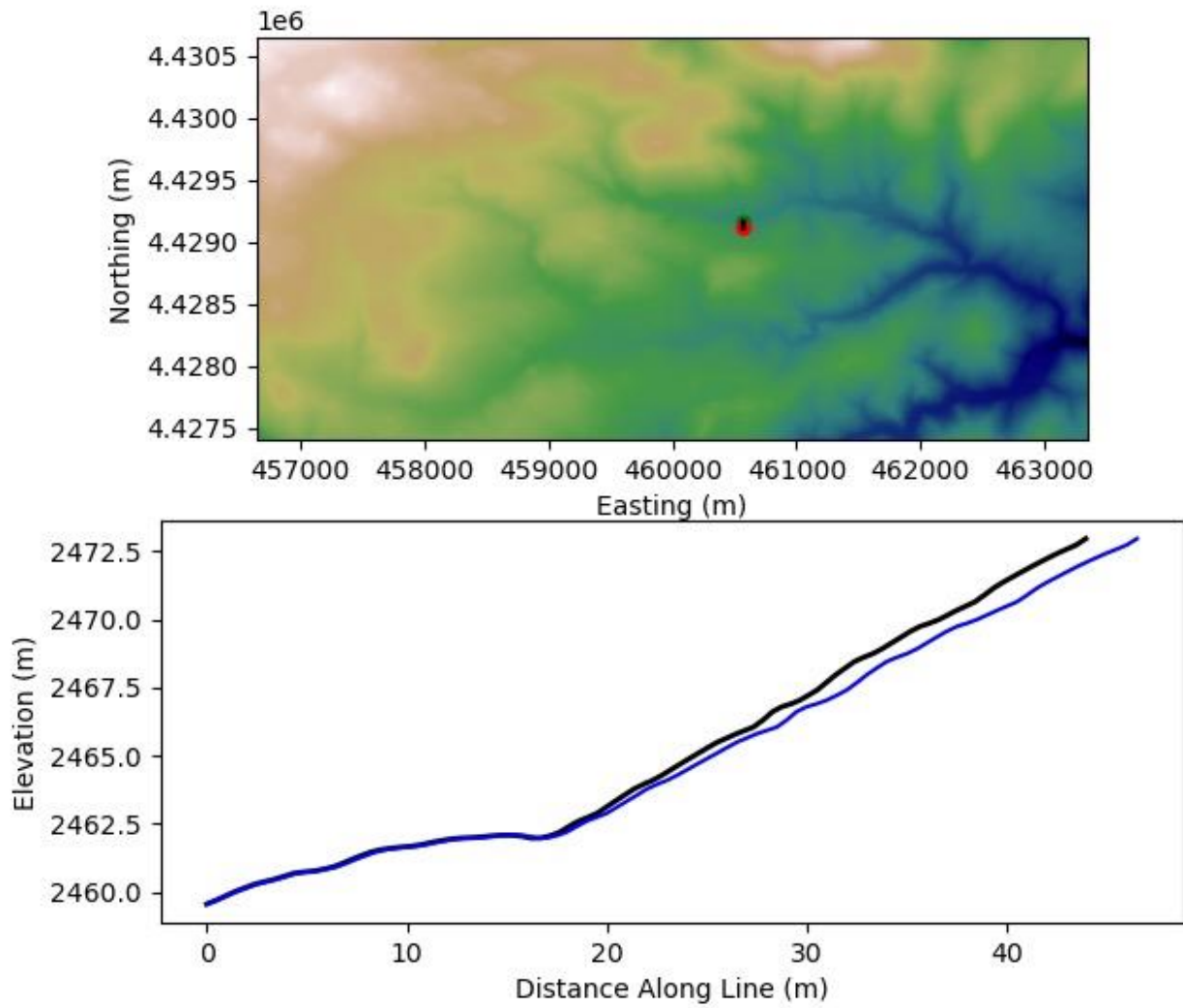


Figure B.9 Elevation profile and distance for seismic Line 3 on the south-facing slope generated by the *extractElevationProfile_rev2.py* script in Anaconda.

Line 3

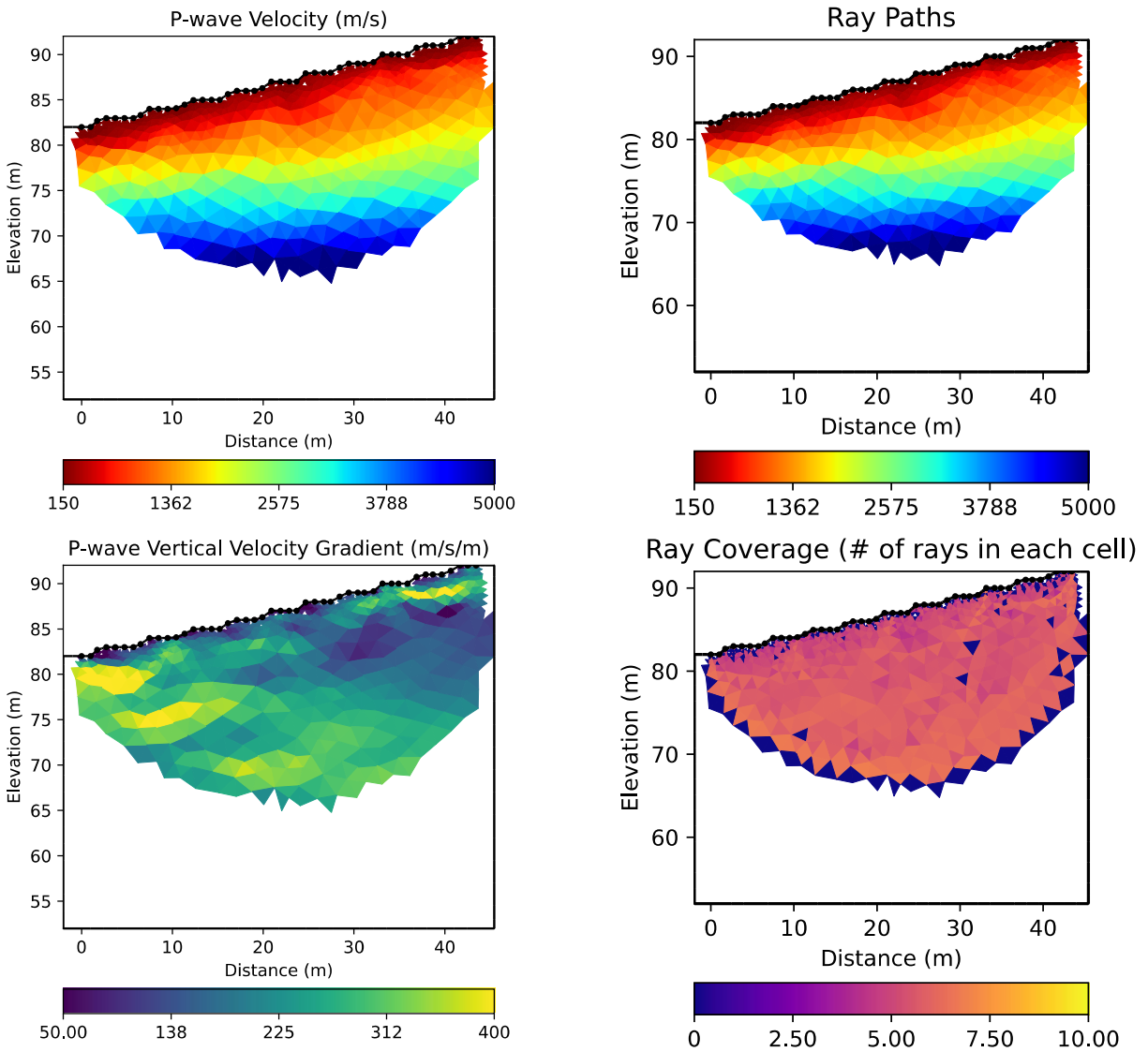


Figure B.10 P-wave velocity profile, p-wave vertical velocity gradient, ray paths, and ray coverage for seismic Line 3 generated by the pyGIMLi inversion using the script *StreamLineInversion_Pwave.py*.

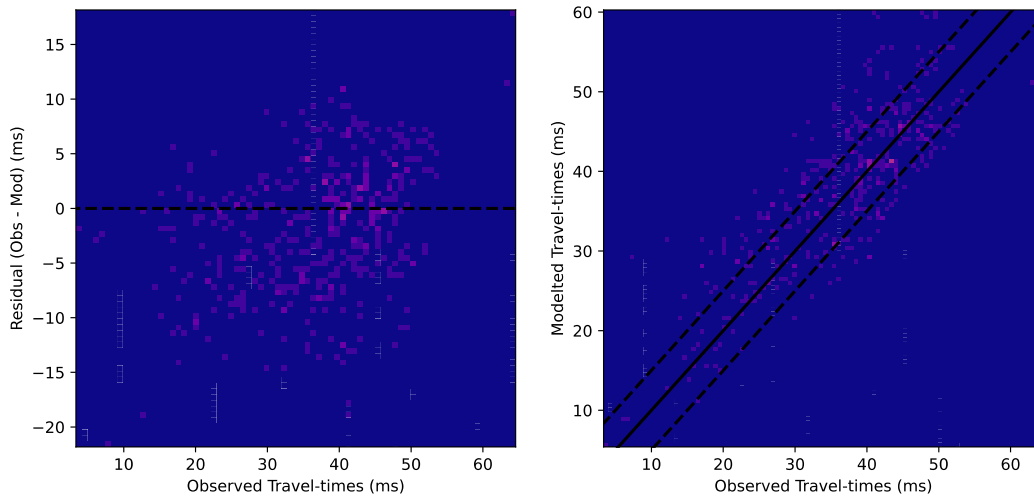


Figure B.11 The residual (observed – modeled) as a function of the observed travel times, and modeled vs observed travel times for seismic Line 3.

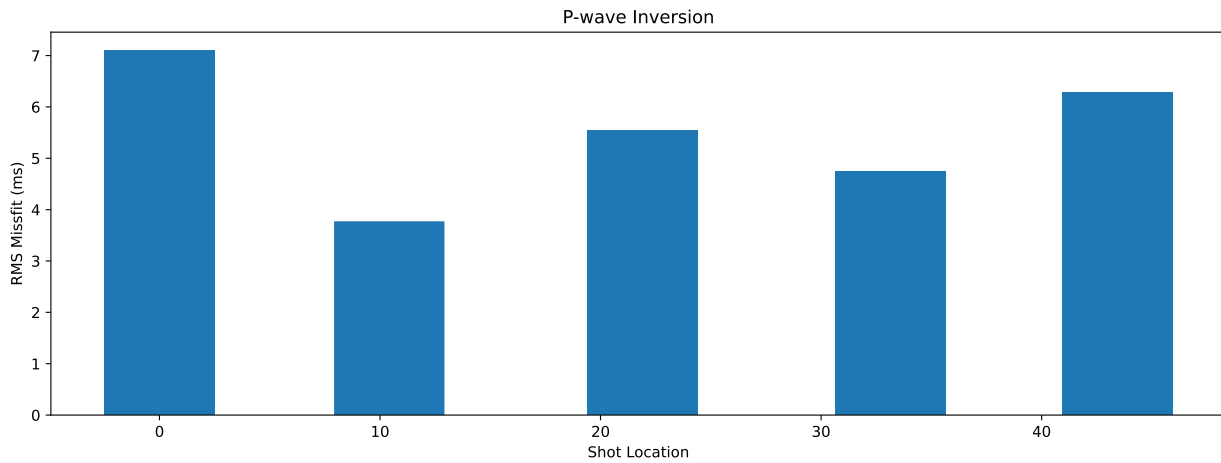


Figure B.12 The root mean square (RMS) misfit for each shot location for the p-wave inversions for Line 3.

Hourly Sap Flow June-September 2021

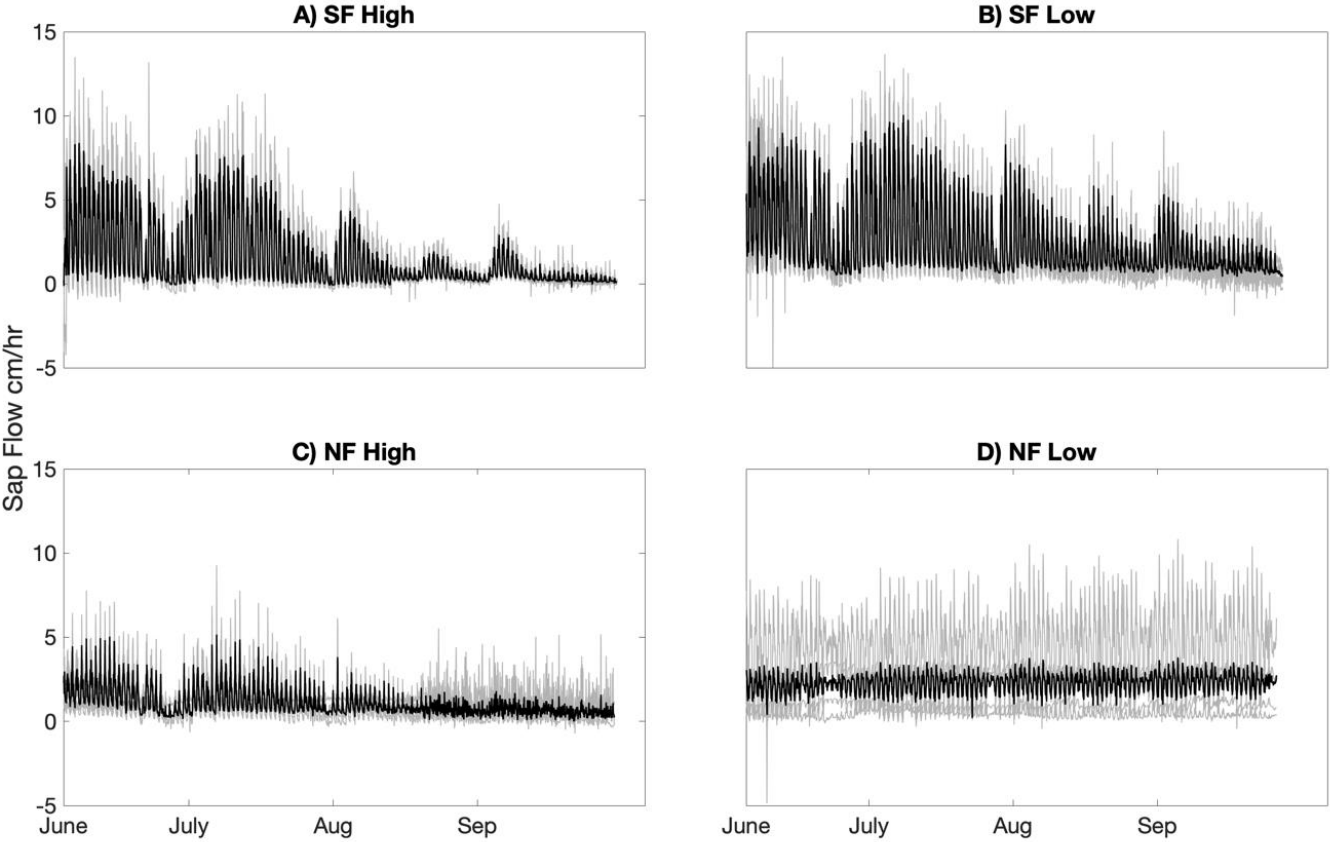


Figure B.13. Hourly sap flow velocities in cm/hr from June to September of 2021 for all four sap flow plots, two on the south-facing slope A) SF_High and B) SF_Low and two on the north-facing slope C) NF_High and D) NF_Low. The gray lines are the sap flow velocities for each individual tree and the black lines are the average of all trees at each plot.

NF Low: North-Facing Downslope Trees 5 & 6

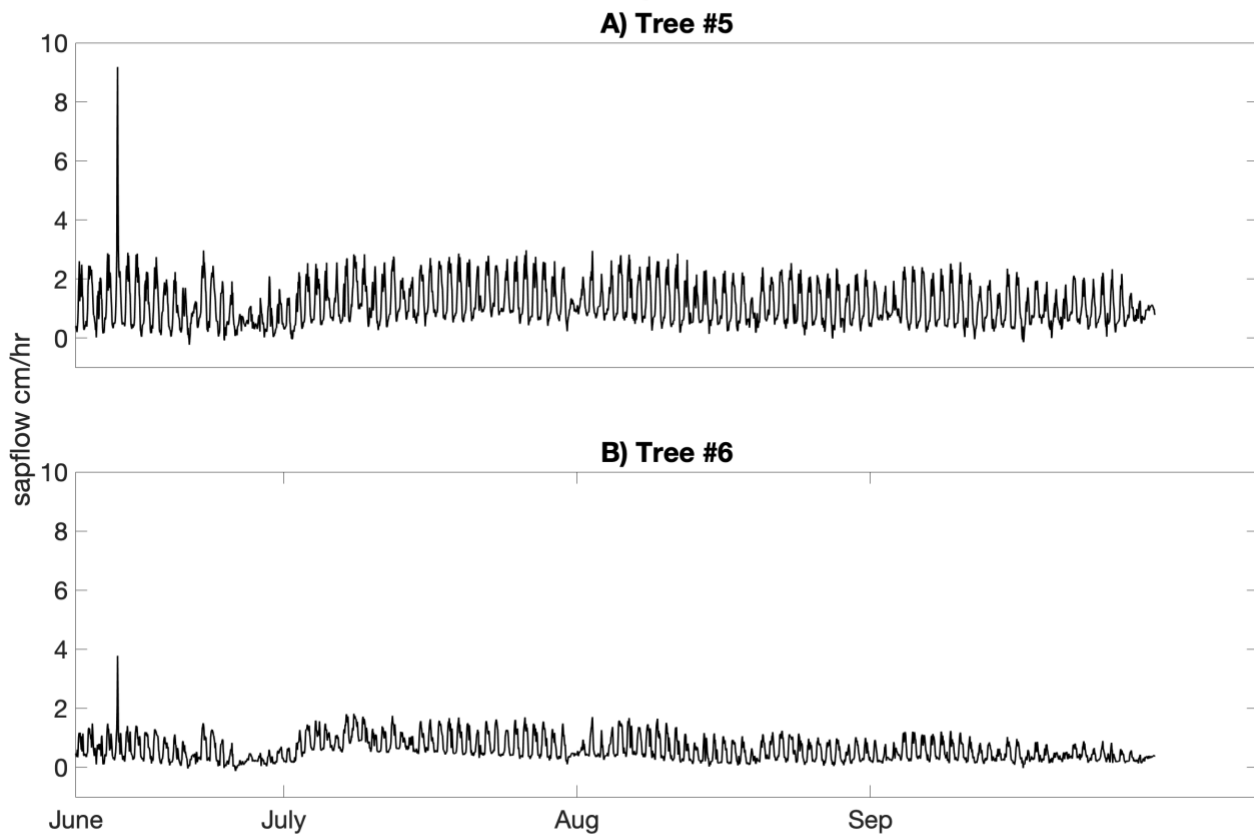


Figure B.14. Hourly sap flow velocity in cm/hr from June to September of 2021 for A) Tree #5 and B) Tree #6 from the NF Low plot or North-Facing Downslope plot. These two trees display slight trends from June-September however as the sap flow data from the rest of the trees at this plot are very noisy, it is difficult to generate meaningful conclusions from just two trees. They have been included here for reference and further study is needed to gather more viable data.

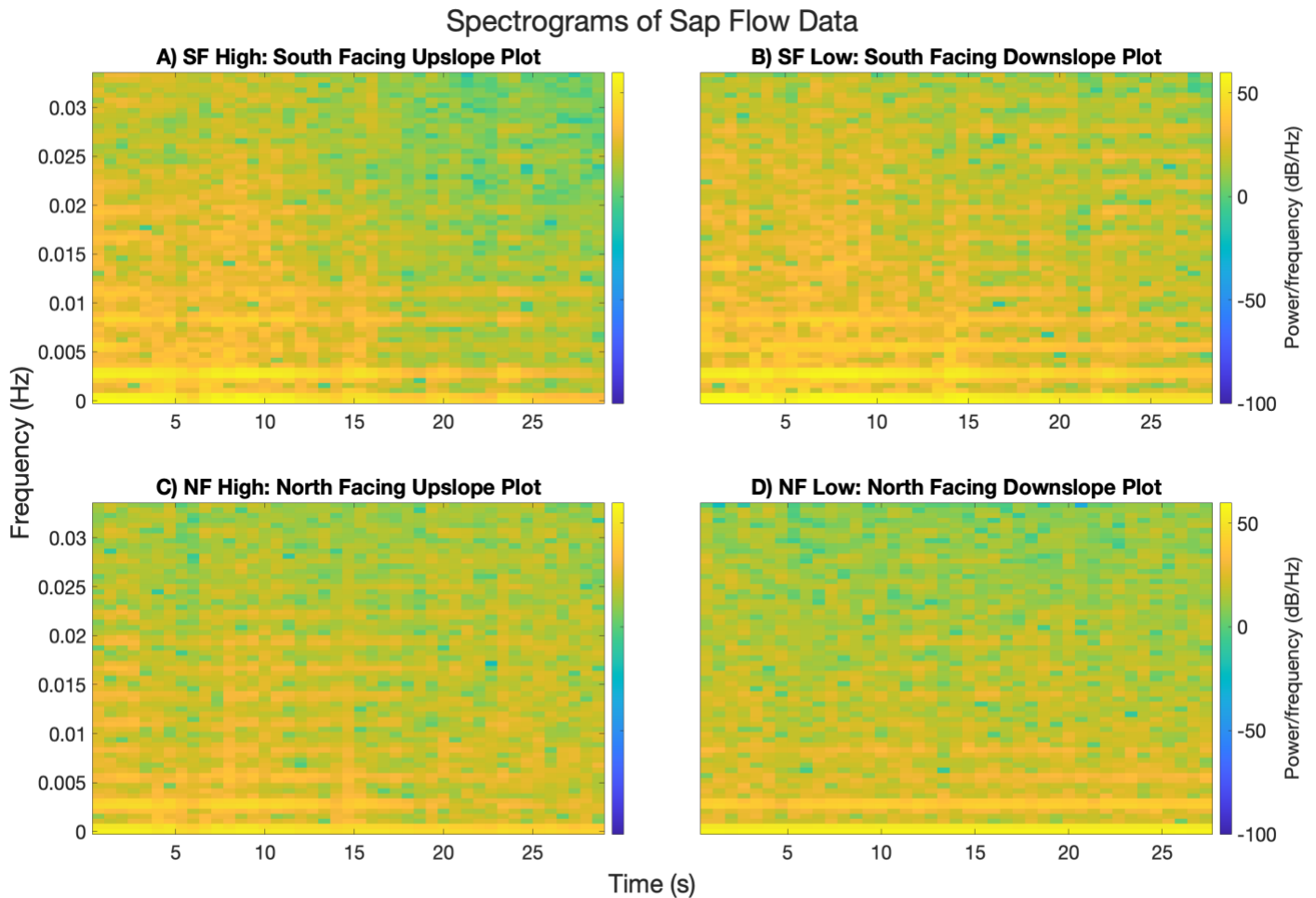


Figure B.15. Spectrograms sap flow plots A) SF High, B) SF Low, C) NF High, and D) NF Low. These plots display the estimated short-term, time-localized content of the provided data. Normalized frequency (Hz) is on the y axis, time (s) is on the x axis, and the color bar indicates frequency intensity. There is no consistent change in dominant frequency with time here, perhaps because sap flow data are always dominated by a diel signal. That said, there is some different in power with time and between hillslopes that might be interesting for future analysis. The MATLAB code used for this graph is as follows: `fs=1/(15*60); %(frequency of data collection in seconds), Nspec=128; %(window length), Noverlap = Nspec/2;, Nfft=Nspec;, spectrogram(Data,Nspec,Noverlap,Nfft,fs,'yaxis');`